



ATLAS CONF Note

ATLAS-CONF-2017-033

16th May 2017



Search for new phenomena with large jet multiplicities and missing transverse momentum using large-radius jets and flavour-tagging at ATLAS in 13 TeV pp collisions

The ATLAS Collaboration

A search is presented for particles that decay producing a large jet multiplicity and invisible particles. The event selection applies a veto on the presence of isolated electrons or muons and additional requirements on the number of b -tagged jets and the scalar sum of masses of large-radius jets. Having explored the full ATLAS 2015-2016 dataset of LHC proton-proton collisions, which corresponds to 36.1 fb^{-1} of data, no evidence is found for physics beyond the Standard Model. The results are interpreted in the context of simplified models inspired by R-parity-conserving and R-parity-violating supersymmetry, where gluinos are pair-produced. More generic phenomenological minimal supersymmetric Standard Model models are also considered.

1 Introduction

As the experiments at the Large Hadron Collider [1] (LHC) continue to amass data from the 13 TeV centre-of-mass energy run, observing the production of heavy resonances remains a principal path to demonstrating physics beyond the Standard Model (BSM), such as supersymmetry. One distinctive signature of such processes would be an increased incidence of events containing a large number of jets accompanied by missing transverse momentum (E_T^{miss}). These could originate from extended cascade decays of heavy particles through lighter states, which might interact weakly and therefore have remained unobserved due to their lower production cross-sections.

A particle spectrum of this nature is exemplified by the pair-production of heavy gluinos (\tilde{g}) that decay via long cascade decays, such as through the superpartners of the electroweak and Higgs bosons. In R-parity-conserving (RPC) [2] SUSY models, these decays culminate in the production of a stable lightest supersymmetric particle (LSP). Cosmological and other observations prohibit an electrically charged or strongly-interacting LSP [3–6], hence the production of these objects, invisible to the detector, would result in missing transverse momentum. Similarly large jet multiplicities could also be achieved if the gluinos were to decay via on- or off-shell top squarks (\tilde{t}_1) or via R-parity-violating (RPV) [7] couplings. In the latter case, the LSP could decay within the detector volume, softening the E_T^{miss} spectrum.

This paper communicates the results of an analysis of 36.1 fb^{-1} of proton-proton (pp) collision data recorded at $\sqrt{s} = 13 \text{ TeV}$ by the ATLAS experiment [8] in 2015 and 2016, scrutinising events that contain at least seven jets with a large transverse momentum (p_T) and significant E_T^{miss} . Selected events are further classified based on the presence of jets containing B -hadrons (b -jets) or on the sum of the masses of large-radius jets. The b -jet selection improves sensitivity to BSM signals with enhanced heavy flavour decays. Given the unusually high jet multiplicities of the target signatures, large jet masses can originate both from capturing the decay products from boosted heavy particles including top quarks and from accidental combinations [9]. A key feature of the search is the data-driven method used to estimate the dominant background from multijet production. Other major background processes include top-quark pair-production ($t\bar{t}$) and W -boson production in conjunction with jets ($W+\text{jets}$).

Previous searches by ATLAS in this final state have been carried out on smaller quantities of LHC data taken at $\sqrt{s} = 8 \text{ TeV}$ from 2011–2012 [10–12] and at $\sqrt{s} = 13 \text{ TeV}$ in 2015 [13]. Due to the more modest selection on E_T^{miss} , this analysis is sensitive to classes of signals not excluded by related searches performed by ATLAS [14–18] and CMS [19–26].

In the next section the ATLAS detector is described, followed by a description of accumulated data and simulated event samples in Section 3. Then the definition of event reconstruction and selection are explained in Section 4 and 5. The data-driven method to estimate QCD multijet background and the estimate of systematic errors are in Section 6 and 7. The result and interpretations are presented in Section 8 followed by conclusions.

2 ATLAS detector

The ATLAS detector [8] at the LHC covers nearly the entire solid angle¹ around the collision point. It consists of an inner tracking detector surrounded by a thin superconducting solenoid, electromagnetic and hadronic calorimeters, and a muon spectrometer incorporating three large superconducting toroid magnets. The inner-detector system (ID) is immersed in a 2 T axial magnetic field and provides charged particle tracking in the range $|\eta| < 2.5$.

The high-granularity silicon pixel detector covers the vertex region and typically provides four measurements per track. It is followed by the silicon microstrip tracker which usually provides four two-dimensional measurement points per track. These silicon detectors are complemented by the transition radiation tracker, which enables radial extension of tracks with $|\eta| < 2.0$. The transition radiation tracker (TRT) also provides electron identification information based on the fraction of hits (typically 30 in total) above a higher energy deposit threshold corresponding to transition radiation.

The calorimeter system covers the pseudorapidity range $|\eta| < 4.9$. Within the region $|\eta| < 3.2$, electromagnetic calorimetry is provided by barrel and endcap high-granularity lead/liquid-argon (LAr) electromagnetic calorimeters, with an additional thin LAr presampler covering $|\eta| < 1.8$, to correct for energy loss in material upstream of the calorimeters. Hadronic calorimetry is provided by the steel/scintillating-tile calorimeter, segmented into three barrel structures within $|\eta| < 1.7$, and two copper/LAr hadronic endcap calorimeters. The solid angle coverage is completed with forward copper/LAr and tungsten/LAr calorimeter modules optimised for electromagnetic and hadronic measurements respectively.

The muon spectrometer (MS) comprises separate trigger and high-precision tracking chambers measuring the deflection of muons in a magnetic field generated by superconducting air-core toroids. The precision chamber system covers the region $|\eta| < 2.7$ with three layers of monitored drift tubes, complemented by cathode strip chambers in the forward region, where the background is highest. The muon trigger system covers the range $|\eta| < 2.4$ with resistive plate chambers in the barrel, and thin gap chambers in the endcap regions.

A two-level trigger system is used to select interesting events [27, 28]. The Level-1 trigger is implemented in low-latency electronics and uses a subset of detector information to reduce the event rate to below 90 kHz. This is followed by a software-based High-Level Trigger which reduces the average event rate to about 1 kHz.

3 Collision data and simulated event samples

Data recorded by ATLAS during 2015 and 2016 have been used in this analysis for background estimation as well as in the final signal region (SR) selections. Simulated events produced with several Monte Carlo (MC) event generators provide predictions for sub-dominant background contributions from Standard Model (SM) processes producing top quarks and vector bosons. The main source of background is multijet production, for which predictions are derived directly from data, as described in Section 6.1.

¹ ATLAS uses a right-handed coordinate system with its origin at the nominal interaction point (IP) in the centre of the detector and the z -axis along the beam pipe. The x -axis points from the IP to the centre of the LHC ring, and the y -axis points upwards. Cylindrical coordinates (r, ϕ) are used in the transverse plane, ϕ being the azimuthal angle around the z -axis. The pseudorapidity is defined in terms of the polar angle θ as $\eta = -\ln \tan(\theta/2)$. Angular distance is measured in units of $\Delta R_y \equiv \sqrt{(\Delta y)^2 + (\Delta \phi)^2}$, where y is the rapidity $1/2 \ln ((E + p_z)/(E - p_z))$.

Models of potential signals are likewise simulated for analysis optimisation and interpretation of the final results.

3.1 Data

Collision events studied for this paper comprise $3.2 \pm 0.07 \text{ fb}^{-1}$ recorded with good data quality in 2015 with a further $32.9 \pm 1.12 \text{ fb}^{-1}$ recorded throughout 2016, all with a bunch spacing of 25 ns. The luminosity uncertainty was derived using beam-separation scans, following a methodology similar to that detailed in Ref. [29]. Pileup, i.e. additional pp interactions in the same or adjacent bunch crossing, contribute to the signals registered by the detector. For this dataset, the average number of interactions per bunch crossing ranged up to 52, with a mean of 22.9.

Events were recorded with a variety of triggers. Throughout 2015 and 2016, a centrally-restricted (jet $|\eta| < 2.4$) trigger requiring at least six jets with $p_T > 45 \text{ GeV}$. In addition, in 2015 events were triggered by requiring the presence of at least five jets with $p_T > 70 \text{ GeV}$ and in 2016 with a centrally-restricted (jet $|\eta| < 2.4$) trigger requiring at least five jets with $p_T > 65 \text{ GeV}$.

Minimum data quality requirements are imposed to ensure that only events are used in which the entire ATLAS detector was functioning well. These, for example, exclude data corruption in the ID and calorimeters, excessive noise and spurious jets produced by non-collision backgrounds [30, 31].

3.2 Simulated event samples

All simulated events are overlaid with multiple pp collisions simulated with the soft QCD processes of PYTHIA 8.186 [32] using the A2 set of parameters [33] and the MSTW2008LO parton distribution functions (PDFs) [34]. The simulated events are weighted such that the pileup conditions match those of the data. The response of the detector to particles is modelled with an ATLAS detector simulation [35] based fully on GEANT4 [36], or using fast simulation based on a parameterisation of the performance of the ATLAS electromagnetic and hadronic calorimeters [37] and on GEANT4 elsewhere.

3.2.1 Background process simulation

For the generation of $t\bar{t}$ and single top-quarks in the Wt and s -channels PowHEG-Box v2 [38–43] was used with the CT10 PDF sets [44] in the matrix element calculations. Electroweak t -channel single top-quark events were generated using PowHEG-Box v1. This generator uses the four-flavour scheme for the next-to-leading-order (NLO) matrix element calculations together with the fixed four-flavour PDF set CT10f4 [44]. For this process, the top quarks are decayed using MADSPIN [45] preserving all spin correlations, while for all processes the parton shower, fragmentation, and the underlying event are simulated using PYTHIA v6.428 [46] with the CTEQ6L1 PDF sets [47] and the Perugia 2012 tune (P2012) [48]. The top quark mass is set to 172.5 GeV. The EvtGEN v1.2.0 program [49] is used to model properties of the bottom and charm hadron decays for this process. Simulated $t\bar{t}$ events are normalised to the cross-section calculated to next-to-next-to-leading-order (NNLO) in perturbative QCD, including soft-gluon resummation to next-to-next-to-leading-log (NNLL) order [50].

Events containing $t\bar{t}$ and additional heavy particles – comprising three-top, four-top, $t\bar{t} + W$, $t\bar{t} + Z$ and $t\bar{t} + WW$ production – are simulated at leading order (LO) in the strong coupling constant α_s , using

`MADGRAPH5` v2.2.2 [51] with up to two additional partons in the matrix element, interfaced to the `PYTHIA` 8.186 parton shower model. The A14 set of `PYTHIA` 8 parameters is used [52], together with the NNPDF2.3 LO PDF set [53]. The predicted production cross-sections are calculated to NLO as described in Ref. [51]. In addition, $t\bar{t} + H$ events are simulated at NLO using `MADGRAPH5_AMC@NLO` v2.3.2 [51], with the NNPDF3.0 NLO PDF set [54] used in the matrix element calculation, and again interfaced to `PYTHIA` 8.186 for the parton shower, with the A14 tune and the NNPDF2.3 LO PDFs.

Events containing W or Z bosons associated with jets are simulated using the `SHERPA` 2.2.1 generator. Matrix elements are calculated for up to two partons at NLO and four partons at LO using the `COMIX` [55] and `OPENLOOPS` [56] matrix element generators and merged with the `SHERPA` parton shower [57] using the `ME+PS@NLO` prescription [58]. The NNPDF3.0 NNLO PDF set is used in association to a tuning performed by the `SHERPA` authors.

Diboson processes with four charged leptons, three charged leptons + one neutrino, two charged leptons and two neutrinos, are simulated using `SHERPA` v2.1.1 [59]. The matrix element calculations contain all diagrams with four electroweak vertices. They are calculated for up to one (for 4ℓ , $2\ell+2\nu$) or without additional partons (for $3\ell+1\nu$) at NLO and up to three additional partons at LO using the `COMIX` and `OPENLOOPS` matrix element generators and merged with the `SHERPA` parton shower using the `ME+PS@NLO` prescription. The `CT10` PDF set is used in conjunction with dedicated parton shower tuning developed by the `SHERPA` authors. An identical procedure is followed to simulate diboson production with one hadronic boson decay accompanied by one charged lepton and one neutrino, two charged leptons or two neutrinos, where the calculations include one additional parton at NLO for $ZZ \rightarrow 2\ell + q\bar{q}$ and $ZZ \rightarrow 2\nu + q\bar{q}$ only, and up to three additional partons at LO.

Theoretical uncertainties are considered on all these simulated samples. By far the most important process simulated in this analysis is $t\bar{t}$ production, and to evaluate the uncertainty on this background several samples are compared. Samples are produced with the factorisation and renormalisation scales varied coherently, along with variations of the h_{damp} parameter in `POWHEG-Box` and with more/less radiation tunes of the parton shower [60]. Additionally, to account for uncertainties in the parton shower modelling and generator choice, the nominal sample is compared to samples generated with `POWHEG-Box` and `MADGRAPH5_AMC@NLO`, interfaced to `HERWIG++` [61]. The comparison with samples which vary the amount of additional radiation contributes the largest uncertainty on the signal region predictions.

Full simulation is used for all background MC samples, ensuring an accurate representation of detector effects. Further details of samples can be found in Refs. [60, 62–65].

3.2.2 Supersymmetric signal models

A number of supersymmetric signal model samples are simulated to permit the interpretation of the search results in terms of supersymmetric parameters. Substantial cross-sections are possible for production of gluinos, superpartners of the gluon, whose cascade decays result in a large multiplicity of jets, which may furthermore exhibit an unusually high heavy-flavour content or atypical substructure.

The first is a simplified model, in which gluinos are pair-produced and then decay the cascade decay:

$$\begin{aligned} \tilde{g} &\rightarrow q + \bar{q}' + \tilde{\chi}_1^\pm \quad (q = u, d, s, c), \\ \tilde{\chi}_1^\pm &\rightarrow W^\pm + \tilde{\chi}_2^0 \\ \tilde{\chi}_2^0 &\rightarrow Z + \tilde{\chi}_1^0, \end{aligned}$$

where the quarks are only permitted to be from the first two generations. The parameters of the model are the masses of the gluino, $m_{\tilde{g}}$, and the lightest neutralino, $m_{\tilde{\chi}_1^0}$. The mass of the $\tilde{\chi}_1^\pm$ is constrained to be $\frac{1}{2}(m_{\tilde{g}} + m_{\tilde{\chi}_1^0})$, and the mass of the $\tilde{\chi}_2^0$ is set to $\frac{1}{2}(m_{\tilde{\chi}_1^\pm} + m_{\tilde{\chi}_1^0})$. A diagram of this “two-step” simplified model is shown in Figure 1(a).

A second type of SUSY model is drawn from a two-dimensional subspace of the 19-parameter phenomenological minimal supersymmetric Standard Model (pMSSM) [66, 67], motivated in part by models not previously excluded in the analysis of Ref. [15]. An example pMSSM process is shown in Figure 1(b). These models are selected to have a bino-like neutralino $\tilde{\chi}_1^0$, kinematically accessible gluinos, and an intermediate-mass Higgsino-like multiplet, containing two neutralinos (the $\tilde{\chi}_2^0$ and $\tilde{\chi}_3^0$) and a chargino (the $\tilde{\chi}_1^\pm$). The masses of these particles are varied by changing the SUSY soft-breaking parameters M_3 (for the gluino) and μ (for the Higgsinos), while M_1 (for the $\tilde{\chi}_1^\pm$) is held constant at 60 GeV. In order that other SUSY particles remain kinematically inaccessible, the other parameters, defined in Ref. [15], are set to $m_A = M_2 = 3$ TeV, $A_\tau = 0$, $\tan \beta = 10$, $A_t = A_b = m_{(\tilde{e}, \tilde{\mu}, \tilde{\tau})L} = m_{(\tilde{e}, \tilde{\mu}, \tilde{\tau})R} = m_{\tilde{q}L(1,2,3)} = m_{(\tilde{u}, \tilde{c}, \tilde{t})R} = m_{(\tilde{d}, \tilde{s}, \tilde{b})R} = 5$ TeV. Mass spectra with consistent electroweak symmetry breaking are generated using SOFTSUSY 3.4.0 [68]. The decay branching ratios are calculated with SDECAY/HDECAY 1.3b/3.4 [69], and when $m_{\tilde{\chi}_1^\pm} \lesssim 500$ GeV and $m_{\tilde{g}} \gtrsim 1200$ GeV the predominant decays are $\tilde{g} \rightarrow t + \bar{t} + \tilde{\chi}_2^0(\tilde{\chi}_3^0)$ and $\tilde{g} \rightarrow t + \bar{b} + \tilde{\chi}_1^\pm$, with $\tilde{\chi}_2^0(\tilde{\chi}_3^0)$ decaying to $Z/h + \tilde{\chi}_1^\pm$ and $\tilde{\chi}_1^\pm$ to $W^\pm + \tilde{\chi}_1^0$. When these decays dominate they lead to final states with many jets, several of which are b -jets, but relatively little E_T^{miss} . This renders this search particularly sensitive compared to most other SUSY searches which tend to require high E_T^{miss} . At higher $m_{\tilde{\chi}_1^\pm}$ and lower $m_{\tilde{g}}$, the decay $\tilde{g} \rightarrow qq\tilde{\chi}_1^0$ becomes dominant and this search starts to lose sensitivity. This model is labelled in the following figures as ‘pMSSM’.

Gluino-mediated stop (\tilde{t}_1) production, with the stops being off-shell, is also a good match for the target final state. This scenario is characterised by the pair-production of gluinos followed by their decay with 100% branching ratio to $t\bar{t} + \tilde{\chi}_1^0$, through a virtual stop particle. Naturalness arguments for supersymmetry favour light gluinos, stops, and Higgsinos, so this final state is very well motivated. Figure 1(c) shows a diagram for the off-shell process.

Permitting non-zero R -parity-violating (RPV) couplings allows consideration of another variation on gluino-mediated stop production, wherein the last step of the decay proceeds via a baryon-number-violating interaction: $\tilde{t}_1 \rightarrow \bar{s} + \bar{b}$ (charge conjugates implied). Figure 1(d) presents the RPV model. Such R -parity-violating models give rise to final states with low missing transverse momentum. Among the strongly-produced supersymmetry searches, the current analysis selects final states with sufficiently low missing transverse momentum to be sensitive to these R -parity-violating scenarios.

The signal samples are generated using **MADGRAPH5_AMC@NLO** v2.2.3 interfaced to **PYTHIA** 8.186 with the A14 tune for the modelling of the parton showering (PS), hadronisation and underlying event. The matrix element (ME) calculation is performed at tree-level and includes the emission of up to two additional partons. The PDF set used for the generation is **NNPDF23LO**. The ME-to-PS matching is done using the CKKW-L prescription [70], with a matching scale set to $m_{\tilde{g}}/4$.

The gluino-mediated stop production signal samples are generated with full simulation of the ATLAS detector, whereas the other signal MC samples employ the fast detector simulation.

Signal cross-sections are calculated to NLO in the strong coupling constant, adding the resummation of soft gluon emission at next-to-leading-logarithmic accuracy (NLO+NLL) [71–75]. The nominal cross

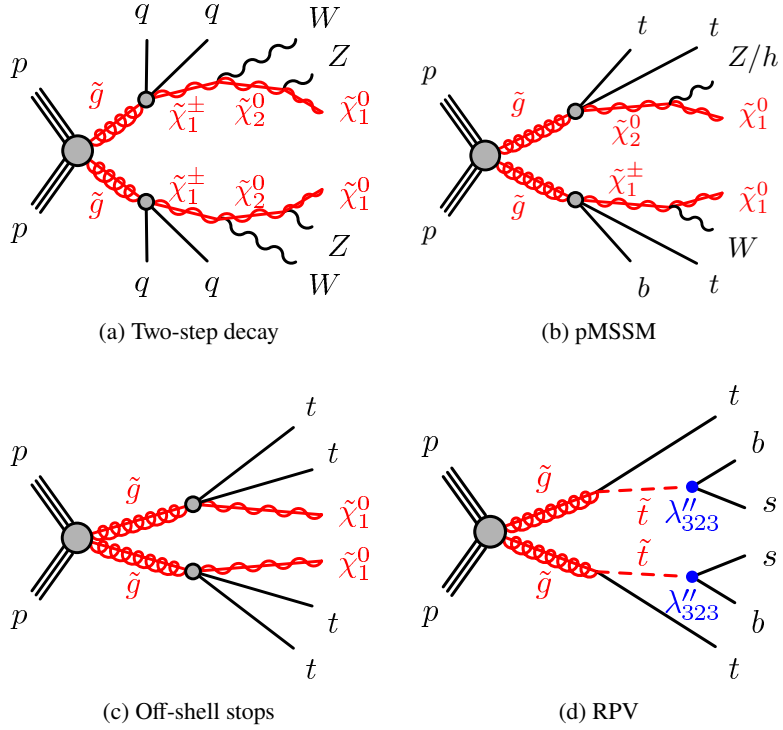


Figure 1: Pseudo-Feynman diagrams for the different signal models used in this search.

section and the uncertainty are taken from an envelope of cross section predictions using different PDF sets and factorisation and renormalisation scales, as described in Ref. [76].

4 Event reconstruction

4.1 Primary vertex

Primary vertices are reconstructed using at least two charged particle tracks with $p_T > 400$ MeV measured by the ID [77]. The primary vertex with the largest sum of squared track transverse momenta ($\sum p_T^2$) is designated the hard scatter vertex.

4.2 Jets

Jets are reconstructed from three-dimensional topological clusters of calorimeter cells (topoclusters) that are noise-suppressed and calibrated to the electromagnetic scale, i.e. corrected for the calorimeter response to electrons and photons [78]. *Small-radius jets* are built by applying the anti- k_t clustering algorithm [79], as implemented in *FastJet* [80], with jet radius parameter $R = 0.4$ to the topoclusters. Four-vector corrections are applied to the jets, starting with a subtraction procedure that removes the average estimated energy contributed by pileup interactions based on the jet area [81]. This is followed by *jet energy scale* calibrations that restore the jet energy to the mean response versus particle-level simulation, using a *global*

sequential calibration to correct finer variations due to flavour and detector geometry and finally *in situ* corrections that match the data to the MC scale [82]. Only jets with $p_T > 20$ GeV and $|\eta| < 2.8$ are considered.

To eliminate jets containing a large energy contribution from pileup, jets are tested for compatibility with the hard scatter vertex with the *jet vertex tagger* (JVT) discriminant, utilising information from the ID tracks associated to the jet [83]. Any jets with $20 < p_T < 60$ GeV and $|\eta| < 2.4$ for which $\text{JVT} < 0.59$ are considered to have been contributed by pileup and are therefore rejected from the analysis. Scale factors derived from data are applied to the event weights for the simulated samples to correct the efficiency of the JVT selection.

A multivariate discriminant (MV2c10) is used to tag jets containing B -hadrons [84] (b -jets). This exploits the long lifetime, high decay multiplicity, hard fragmentation and large mass of b -hadrons. The selected working point for the b -tagging algorithm [85] tags b -jets with an efficiency of approximately 70% in simulated $t\bar{t}$ events, and rejects c -jets, τ -jets and light-quark or gluon jets by factors of 9.6, 31 and 254, respectively. For the purposes of overlap removal, a *loose b-tag* designation is defined using a working point with 80% b -tagging efficiency. Where b -tagging selections are applied, efficiency corrections measured in data are applied to simulated events, to improve modelling of the b -tagging efficiencies.

In a second jet *reclustering* step [86], small-radius jets with $p_T > 20$ GeV and $|\eta| < 2.8$ are combined using the anti- k_t algorithm with radius parameters $R = 1.0$ to form *large-radius jets*. The input jets are required to pass an overlap removal procedure accounting for ambiguities between jets and leptons, as discussed below. In the leptonic control region (CR) defined in Section 5.2, electrons and muons may also be included in the inputs to the jet reclustering provided they satisfy $p_T > 20$ GeV and $|\eta| < 2.0$ as for standard jets. Large-radius jets are retained for analysis if they have $p_T > 100$ GeV and $|\eta| < 1.0$.

4.3 Electrons and photons

Candidates of electrons and photons are reconstructed from clusters of calorimeter cells defined with fixed rectangular η - ϕ sizes and then distinguished by matching to ID tracks [87, 88]. The fine η granularity and longitudinal segmentation of the electromagnetic calorimeter allow rejection of backgrounds from hadron and jets. A multivariate calibration is applied to correct the electron/photon energy scale [89].

Electron candidates are preselected if they have $p_T > 10$ GeV, $|\eta| < 2.47$ and pass a “Loose” likelihood-based quality selection accounting for lateral shower shapes, hadronic shower leakage, hits on track, track-cluster matching and the number of high-threshold hits in the TRT. Signal electrons with $p_T > 25$ GeV are defined by requiring a “Tight” likelihood selection including impact parameter restrictions and the “GradientLoose” isolation requirement from Ref. [90] in addition to the preselection. To achieve additional rejection of background electrons from non-prompt sources, signal electron tracks must be matched to the hard scatter vertex with longitudinal impact parameter $|z_0| < 0.5$ mm and transverse impact parameter significance $|d_0|/\sigma(d_0) < 5$. Corrections to the electron reconstruction and identification efficiency in simulated samples are applied using scale factors measured in data [90].

Photon candidates likewise are identified using tight criteria defined by lateral shower shapes in the first and second layers of the electromagnetic calorimeter, as well as the degree of hadronic shower leakage. Acceptance requirements of $p_T > 25$ GeV and $|\eta| < 2.37$ are applied.

4.4 Muons

Muon candidates are reconstructed from tracks formed in the ID and MS, which are combined for improved precision and background rejection [91]. Standalone muon tracks are used to extend the muon reconstruction coverage beyond the ID acceptance in pseudorapidity (from $|\eta| > 2.5$ up to $|\eta| = 2.7$).

Preselected muons are defined by a “medium” selection using the number of hits on track and track quality and compatibility between the ID and MS measurements. These must have $p_T > 10$ GeV and $|\eta| < 2.7$. Signal muons must have a higher transverse momentum, $p_T > 25$ GeV, and satisfy the “GradientLoose” isolation requirement [91], as well as impact parameter matching requirements similar to those for electrons: $|z_0| < 0.5$ mm and $|d_0|/\sigma(d_0) < 3$. Muon reconstruction and identification efficiencies are corrected with scale factors in simulated samples [92].

4.5 Overlap removal

To avoid double counting, overlap removal was applied to jets, photons and leptons according to the following procedure. The electrons and muons are those passing the preselection.

1. If an electron and a muon share an ID track, the electron is removed and the muon is retained.
2. Photons that are within $\Delta R_y < 0.4$ of an electron or a muon are deselected.
3. Then, any jet that fails the loose b -tag selection is removed if either:
 - it falls within $\Delta R_y < 0.2$ of an electron; or
 - it has no more than three tracks with $p_T > 500$ MeV, or contains an ID track matched to a muon such that $p_T^{\text{jet}} < 2p_T^{\mu}$ and the muon track has more than 70% of the sum of the transverse momenta of all tracks in the jet, such that the jet resembles radiation from the muon.
4. Any electrons or muons within $\Delta R_y < 0.4$ of a surviving jet are eliminated.
5. Finally, jets that are within $\Delta R_y < 0.4$ of photons are removed.

4.6 Missing transverse momentum

The missing transverse momentum, E_T^{miss} , is defined as the magnitude of the negative vector sum of the transverse momenta of preselected electrons and muons, photons and jets, to which is added a soft term [93]. The soft term is constructed from all tracks that are not associated with any of the preceding objects, and that are associated to the primary vertex. In this way, the missing transverse momentum is adjusted for the best calibration of the leptons, photons and jets, while maintaining pileup independence in the soft term.

5 Event selection

Target signal events for this analysis are characterised by a large jet multiplicity, beyond what is generated by high-cross-section SM processes, combined with a E_T^{miss} that is significantly larger than that expected purely from detector resolution. Several signal regions are defined that select a minimum jet multiplicity and further require a large value of $E_T^{\text{miss}}/\sqrt{H_T}$, where H_T is the scalar sum over jet transverse momenta

$$H_T = \sum_j p_T^j, \quad (1)$$

the sum being restricted to jets with $p_T > 40$ GeV, $|\eta| < 2.8$. This ratio is approximately proportional to the significance of the E_T^{miss} , under the assumption that the expected E_T^{miss} is zero and resolution of the E_T^{miss} originates entirely from the stochastic variation in the jet momentum measurement. For jets with $p_T \lesssim 1$ TeV, the relative jet resolution scales as $1/\sqrt{p_T}$.

Several auxiliary measurements are carried out in control and validation regions (VR) in order to define and constrain the major backgrounds to the analysis. Events selected at a lower jet multiplicity are used to extract the shape of the $E_T^{\text{miss}}/\sqrt{H_T}$ distribution, which is then extrapolated to the signal regions to quantify the multijet background, as described fully in Section 6.1. The normalisation of the $t\bar{t}$ and W +jets background components is adjusted to match data in control regions, using the procedure defined in Section 6.2.

5.1 Signal region definitions

The common selection of events for the signal regions is as follows: To limit the contribution of SM background processes in which neutrinos are produced, leading to significant E_T^{miss} , events containing any preselected electron or muon following overlap removal are rejected. Biases in the E_T^{miss} due to pileup jets surviving the JVT selection are removed by excluding events for which a jet with $60 < p_T < 70$ GeV and $\text{JVT} < 0.59$ lies opposite to the E_T^{miss} ($\Delta\phi(j_i, E_T^{\text{miss}}) > 2.2$). Likewise, events are rejected if they contain a jet with $p_T > 50$ GeV and $|\eta| < 2.0$ pointing towards regions in which tile calorimeter modules were disabled.

Subsequently, restrictions on the jet multiplicity N_{jet} are imposed, depending on the analysis channel; only jets with $p_T > 50(80)$ GeV and $|\eta| < 2.0$ are considered as *signal jets* and therefore used in the N_{jet} selection. These selections are abbreviated as $j50$ ($j80$), for which the corresponding jet multiplicities are denoted N_{jet}^{50} and N_{jet}^{80} . The lower and higher jet p_T thresholds were optimised to permit sensitivity to a variety of potential SUSY mass spectra.

A threshold of $E_T^{\text{miss}}/\sqrt{H_T} > 5$ GeV $^{1/2}$ is the last element of the common selection. This criterion eliminates the vast majority of SM multijet and other background events with low E_T^{miss} , while retaining sensitivity to a broad range of potential signals.

Next, the SRs in the two channels of the analysis are defined by a further categorisation of events.

Criterion	Heavy flavour channel		Jet mass channel
Jet $ \eta $	< 2.0		
Jet p_T	$> 50 \text{ GeV}$	$> 80 \text{ GeV}$	$> 50 \text{ GeV}$
N_{jet}	$\geq 8, 9, 10, 11$	$\geq 7, 8, 9$	$\geq 8, 9, 10$
Lepton veto	No preselected e or μ after overlap removal		
b -jet selection	$p_T > 50 \text{ GeV}, \eta < 2.0$		
Large-R-jet selection	$p_T > 100 \text{ GeV}, \eta < 1.0$		
$N_{b\text{-tag}}$	$\geq 0, 1, 2$		≥ 0
M_J^Σ	≥ 0		$\geq 340, 500 \text{ GeV}$
$E_T^{\text{miss}}/\sqrt{H_T}$	$> 5 \text{ GeV}^{1/2}$		

Table 1: Summary of selection criteria for all signal regions used in this analysis.

5.1.1 Heavy flavour channel

The following N_{jet} values are considered in this channel: minimum $N_{\text{jet}}^{50} \in \{8, 9, 10, 11\}$, and minimum $N_{\text{jet}}^{80} \in \{7, 8, 9\}$. Motivated by the likelihood of heavy flavour jets being produced from cascade decays, three signal regions that respectively require $N_{b\text{-tag}} \geq 0, 1, 2$ are defined for each value of N_{jet} , where the b -jets must have $p_T > 50 \text{ GeV}$ and $|\eta| < 2.0$.

5.1.2 Jet mass channel

Should sparticles be produced and decay through a long decay chain, or provide enough kinetic energy to significantly boost heavy particles such as top quarks and bosons, signal events might be characterised not only by an unusually large jet multiplicity but also by the formation of large-radius jets with high masses. The kinematic structure of SM events, by contrast, does not produce a high rate of events containing large-radius jets with mass greater than the top mass.

For background discrimination in this channel, the selection variable M_J^Σ is defined to be the sum of the masses $m_j^{R=1.0}$ of the composite jets

$$M_J^\Sigma = \sum_j m_j^{R=1.0} \quad (2)$$

where the sum is over the composite jets that satisfy $p_T^{R=1.0} > 100 \text{ GeV}$ and $|\eta^{R=1.0}| < 1.5$, as described in Section 4. Two thresholds on M_J^Σ , chosen following optimisation studies, at 340 GeV and 500 GeV define signal regions for $N_{\text{jet}}^{50} \in \{8, 9, 10\}$, while no $j80$ SRs are defined. As these thresholds are approximately twice and thrice the top mass, their main irreducible backgrounds are respectively top-quark associated production with vector bosons and four-top processes, both of which have a very small rate.

A summary of all signal region selections is given in Table 1.

5.2 Control region definitions

For each signal region, three control regions are used to constrain the background predictions using data, which are split into two sets. The first set, referred to as the *multijet template region* (TR) selection, maintains the same lepton veto as used in the SR, but modifies the signal jet multiplicity or $E_T^{\text{miss}}/\sqrt{H_T}$ selection. Secondly, a pair of *leptonic control regions* are defined, split by b -tagging, in which the lepton veto is replaced with a requirement on the presence of exactly one signal electron or muon (henceforth referred to merely as “lepton”, ℓ).

5.2.1 Multijet template region

Fundamental to this analysis is the extraction of an estimate of the multijet background directly from data, avoiding large theoretical uncertainties on the inclusive and differential cross-sections for these processes. The full estimation procedure is described in Section 6.1.

Broadly, four different selections are used to define the background prediction and its associated systematic uncertainties. The shape of the full $E_T^{\text{miss}}/\sqrt{H_T}$ distribution ($E_T^{\text{miss}}/\sqrt{H_T}$ template) is measured in events containing exactly six signal jets with $p_T > 50$ GeV for the $j50$ signal regions and exactly five signal jets with $p_T > 80$ GeV for the $j80$ signal regions. For normalisation of the template prediction, events are counted in a TR defined by an equal signal jet multiplicity to the signal region, but an upper bound of 1.5 GeV $^{1/2}$ on the $E_T^{\text{miss}}/\sqrt{H_T}$ variable. Validation regions are defined that require seven signal jets with $p_T > 50$ GeV for the $j50$ signal regions and six signal jets with $p_T > 80$ GeV for the $j80$ signal regions, and furthermore impose a minimum 5 GeV $^{1/2}$ threshold, as in the signal regions. Finally, an additional validation region is defined in the range $1.5 < E_T^{\text{miss}}/\sqrt{H_T} < 4.5$ GeV $^{1/2}$, for each signal region jet multiplicity. The same $N_{b\text{-tag}}$ and M_j^{Σ} thresholds are applied in each template and validation region as in the corresponding signal region.

5.2.2 Leptonic control regions

Also important is the estimation of the next two largest background processes, $t\bar{t}$ and $W+\text{jets}$, from MC simulation, as detailed in Section 3.2.1. To correct for potential mismodelling of the process cross-sections and kinematics by the event generators, the normalisation for the background predictions is modified based on a simultaneous fit of the auxiliary measurements, explained in Section 6.3.

The leptonic control regions constraining the $t\bar{t}$ and $W+\text{jets}$ normalisation are defined with identical selection criteria as their corresponding signal regions, apart from the following differences, summarised also in Table 2:

1. Instead of rejecting events containing a preselected lepton, events must contain exactly one signal lepton with $p_T > 20$ GeV.
2. To prevent contamination from potential signals, events must satisfy a requirement on the transverse mass $m_T < 120$ GeV, where

$$m_T = \sqrt{2p_T^\ell E_T^{\text{miss}} \left[1 - \cos(\Delta\phi(\vec{p}_T^\ell, \vec{E}_T^{\text{miss}})) \right]}. \quad (3)$$

3. To increase event counts, the minimum signal jet multiplicity N_{jet} is reduced by one from the corresponding signal region. However, if the lepton satisfies the p_{T} and η requirements imposed on signal jets, then it is treated as a signal jet for the purposes of this selection.
4. Events consistent with $W+\text{jets}$ and $t\bar{t}$ production are separated by means of the $N_{b\text{-tag}}$ selection; the $W+\text{jets}$ CR requires $N_{b\text{-tag}} = 0$ while the $t\bar{t}$ CR requires $N_{b\text{-tag}} \geq 1$.
5. The $E_{\text{T}}^{\text{miss}}/\sqrt{H_{\text{T}}}$ threshold may be lowered from 5 $\text{GeV}^{1/2}$ to 3 $\text{GeV}^{1/2}$ or 4 $\text{GeV}^{1/2}$ where necessary to increase the statistical precision of the measurement. The $E_{\text{T}}^{\text{miss}}/\sqrt{H_{\text{T}}}$ thresholds are specified in Table 3.

Control regions	
Lepton multiplicity	Exactly one signal e or μ
Lepton p_{T}	$> 20 \text{ GeV}$
m_{T}	$< 120 \text{ GeV}$
Jet $p_{\text{T}}, \eta $	Same as SR
Number of jets including lepton	$N_{\text{jet}}^{\text{SR}} - 1$
b-jet multiplicity	$= 0 (W+\text{jets})$ or $\geq 1 (t\bar{t})$
M_{J}^{Σ}	Same as SR
$E_{\text{T}}^{\text{miss}}/\sqrt{H_{\text{T}}}$	$> 3, 4, 5 \text{ GeV}^{1/2}$

Table 2: Definition of the leptonic control regions, used to normalise the $t\bar{t}$ and $W+\text{jets}$ backgrounds. In the control regions, the lepton is recast as a jet if it passes the same kinematic criteria as the jets. Such leptons contribute to the $E_{\text{T}}^{\text{miss}}/\sqrt{H_{\text{T}}}$ (through the H_{T}) and also M_{J}^{Σ} .

Signal channel	Minimum SR N_{jet}		$E_{\text{T}}^{\text{miss}}/\sqrt{H_{\text{T}}}$ threshold
Heavy flavour channel	Jet $p_{\text{T}} > 50 \text{ GeV}$	Jet $p_{\text{T}} > 80 \text{ GeV}$	
	8, 9	7	$> 5 \text{ GeV}^{1/2}$
	10	8	$> 4 \text{ GeV}^{1/2}$
	11	9	$> 3 \text{ GeV}^{1/2}$
Jet mass channel	$M_{\text{J}}^{\Sigma} > 340 \text{ GeV}$	$M_{\text{J}}^{\Sigma} > 500 \text{ GeV}$	
	8	-	$> 5 \text{ GeV}^{1/2}$
	9	8	$> 4 \text{ GeV}^{1/2}$
	10	9, 10	$> 3 \text{ GeV}^{1/2}$

Table 3: The $E_{\text{T}}^{\text{miss}}/\sqrt{H_{\text{T}}}$ thresholds for the control regions corresponding to each signal region. In each case, the same $E_{\text{T}}^{\text{miss}}/\sqrt{H_{\text{T}}}$ threshold is used for both the $W+\text{jets}$ and $t\bar{t}$ control regions.

6 Background estimation techniques

6.1 Multijet template estimation

Accurate modelling of multijet processes from QCD calculations and matrix-element MC event generation is difficult. This is compounded by the challenges of reproducing events populating the tails of the detector

response, representative of the high- E_T^{miss} events selected in this analysis. Hence, to confidently estimate the multijet background component, which makes up 50-70% of the total SM expectation, the prediction is based on direct measurements in data.

The strategy used in this analysis is based on the observation that the $E_T^{\text{miss}}/\sqrt{H_T}$ spectrum for selected multijet events is primarily determined by the calorimeter response to jets, which is approximately independent of how the total jet transverse energy H_T is partitioned between the jets. Thus, the $E_T^{\text{miss}}/\sqrt{H_T}$ spectrum measured in events with a lower jet multiplicity does not greatly differ from that observed in a high jet multiplicity selection. A *template* for the multijet $E_T^{\text{miss}}/\sqrt{H_T}$ distribution can thus be extracted in a selection complementary to the signal region, specifically the template regions defined in Section 5.2.1, permitting a blind analysis. At larger values of $E_T^{\text{miss}}/\sqrt{H_T}$, it is necessary to subtract from the data expected contributions due to SM processes producing neutrinos; this is done using predictions from MC simulation. This template also accounts for smaller background contributions from $t\bar{t}$ production with fully hadronic decays as well as $\gamma + \text{jets}$.

By the logic above, the multijet prediction n_{multijet} for the number of events with $b < E_T^{\text{miss}}/\sqrt{H_T} < c$ for a SR based on a TR can be written as follows:

$$n_{\text{multijet}}^{\text{SR}, b < E_T^{\text{miss}}/\sqrt{H_T} < c} = \frac{n_{\text{multijet}}^{\text{SR}, E_T^{\text{miss}}/\sqrt{H_T} < a}}{n_{\text{multijet}}^{\text{TR}, E_T^{\text{miss}}/\sqrt{H_T} < a}} \cdot n_{\text{multijet}}^{\text{TR}, b < E_T^{\text{miss}}/\sqrt{H_T} < c} \quad (4)$$

$$= \frac{n_{\text{multijet}}^{\text{SR}, E_T^{\text{miss}}/\sqrt{H_T} < a}}{n_{\text{multijet}}^{\text{TR}, E_T^{\text{miss}}/\sqrt{H_T} < a}} \cdot \left(n_{\text{obs}}^{\text{TR}, b < E_T^{\text{miss}}/\sqrt{H_T} < c} - n_{\text{MC}\nu}^{\text{TR}, b < E_T^{\text{miss}}/\sqrt{H_T} < c} \right). \quad (5)$$

The normalisation of the template is fixed in the range $E_T^{\text{miss}}/\sqrt{H_T} < a$ such that $a < b < c$, which is entirely dominated by multijet events. In the template region, the observation in data is denoted n_{obs} , while the predicted number of events with neutrinos is written $n_{\text{MC}\nu}$.

While the exact division of H_T between the multiple jets in a single event does not significantly influence the template independence, the distribution of H_T itself is forced higher as the N_{jet} requirements are made more stringent. This implies an indirect correlation between the $E_T^{\text{miss}}/\sqrt{H_T}$ and the jet multiplicity, contradicting the assumption of template independence. It is therefore necessary to extract the multijet template in several bins of H_T . The lower bin boundaries are set at 0, 600, 900 and 1200 GeV, which was found to be sufficient to remove the dependence of the template on H_T . Predictions for each bin are derived independently and summed to produce the total SR expectation.

Pileup inflates the jet resolution and consequently the scaling of the E_T^{miss} resolution with H_T . The template method integrates over the full pileup distribution in data, thereby accounting for this dependence, as the signal regions do not show a disproportionate efficiency for high-pileup events relative to the template region.

Several factors may influence the accuracy of the multijet template prediction. The majority among these are kinematic variations between the template and signal regions, and differences in the amount of heavy-flavour jets in the two event selections. Systematic uncertainties that estimate the sensitivity of the template prediction to these variables are assessed.

Kinematic differences are covered by comparing the nominal estimate to the prediction extracted using an alternative H_T -binning strategy, setting the bin boundaries instead at 0, 600, 800, 1000, 1200 and 1400 GeV. The resulting uncertainty is typically 5-10% in the SRs.

An uncertainty due to jet flavour composition is determined as the difference between the nominal estimate, which assumes an identical flavour composition between the TR and SRs, and a χ^2 fit that interpolates between the nominal estimate and a *flavour-split* template estimate. The flavour-split template prediction is produced by separating the template and signal regions into two bins, one requiring exactly as many b -jets as in the SR $N_{b\text{-tag}}$ selection, and the latter requiring at least one more. A χ^2 fit to data in the validation regions is then used to linearly combine the nominal and flavour-split templates. The resulting combined template is used as a basis for comparison to the nominal prediction. This procedure ensures that an appropriate uncertainty is estimated if the nominal estimate is significantly different from the best-fit; if the naïve flavour-split estimate describes the data poorly, this does not result in an overestimate of the uncertainty. For the jet mass channel, this uncertainty ranges from 3–6%. It is larger in the heavy flavour channel: at most 20% in the tightest selections, and up to 12% elsewhere.

Finally, to account for other potential sources of mismodelling, an overall closure uncertainty is computed. This is defined as the maximal relative difference between the template prediction and the observation in data for the VRs defined in Section 5.2.1, either with a lower jet multiplicity or a reduced $E_T^{\text{miss}}/\sqrt{H_T}$ value. The template closure is checked in a VR at a lower jet multiplicity but with the same $E_T^{\text{miss}}/\sqrt{H_T} > 5 \text{ GeV}^{1/2}$ threshold as in the SR, or in several bins of $E_T^{\text{miss}}/\sqrt{H_T}$:

$$E_T^{\text{miss}}/\sqrt{H_T} \in (1.5, 2.0), (2.0, 3.0), (3.0, 4.0) \text{ GeV}^{1/2}.$$

Example distributions of $E_T^{\text{miss}}/\sqrt{H_T}$ in the lower-jet-multiplicity VRs are shown in Figure 2. The degree of closure varies, generally ranging between 8–12% and extending to 30% for regions with the lowest statistics.

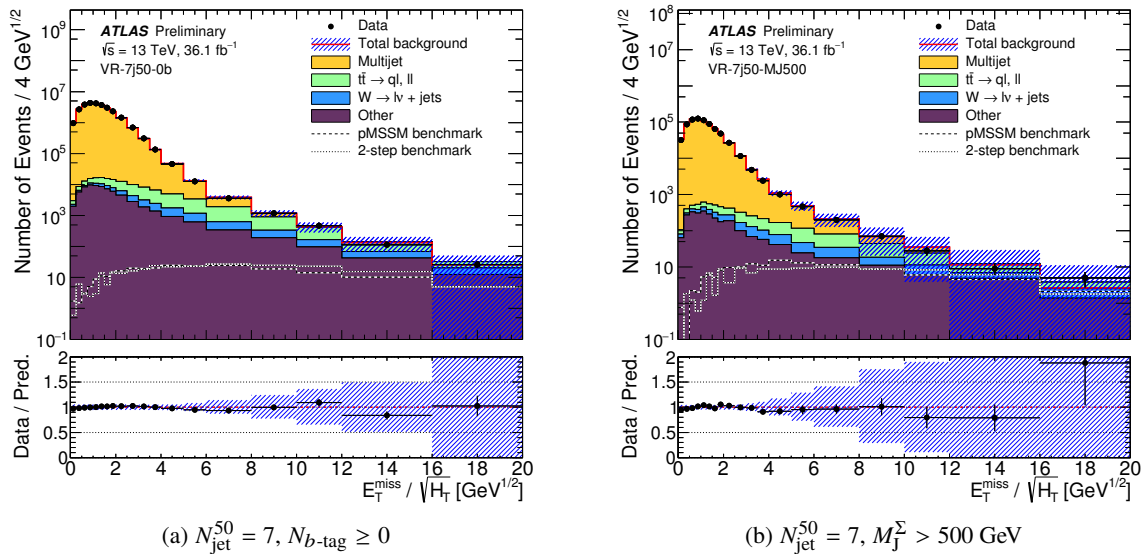


Figure 2: Distributions of the $E_T^{\text{miss}}/\sqrt{H_T}$ for events in the validation regions for a 50 GeV flavour channel selection (a) and a M_J^Σ selection (b). The blue hashed band indicates the quadrature sum of the statistical uncertainty from MC simulated samples and the separate sources of systematic uncertainty on the background prediction. The dashed lines labelled ‘pMSSM’ and ‘2-step’ refer to benchmark signal points – a pMSSM slice model with $(m_{\tilde{g}}, m_{\tilde{\chi}_1^\pm}) = (1400, 200) \text{ GeV}$ and a cascade decay model with $(m_{\tilde{g}}, m_{\tilde{\chi}_1^0}) = (1400, 200) \text{ GeV}$. The lower panels show the ratio of the observed data to the total SM background.

6.2 Leptonic background estimates

All background contributions from processes in which $W \rightarrow \ell\nu$ or $Z \rightarrow \nu\nu$ decays produce neutrinos, including single- or pair-production of top quarks and electroweak vector bosons, are estimated using MC simulation. The two largest of these, $t\bar{t}$ and W +jets, are responsible for 20-45% and up to 10% of the SM background respectively. Other processes, such as Z +jets, single top and diboson production collectively make up no more than 12% of the total SR expectation. As such, corrections to the size of the $t\bar{t}$ and W +jets background components, together with the multijet template estimate previously described, provide a sufficiently accurate background prediction for this search. For each of the $t\bar{t}$, W +jets and multijets background processes, a normalisation factor μ is determined, based on a likelihood fit described in Section 6.3.

Control regions defined as in Section 5.2.2 provide enriched samples of events from the relevant processes, in a kinematic region close to the signal selection. The purity of the CRs is in the vicinity of 85% for $t\bar{t}$ and typically 25-50% for W +jets. As only these two processes contribute substantially to the CR populations, this level of purity is adequate to constrain the normalisations for both well.

Distributions of the number of jets ($p_T > 20$ GeV, $|\eta| < 2.8$) are shown below in Figure 3 for a selection of the $t\bar{t}$ and W +jets CRs.

6.3 Combined background fits

For each background process constrained by the fit, an unconstrained normalisation factor μ_b , $b \in \{t\bar{t}, W, \text{multijet}\}$ is defined, such that $\mu_b = 1$ implies consistency with the nominal MC cross-sections for $t\bar{t}$ and W +jets. The normalisation factor μ_{multijet} allows the MC subtraction applied in the template estimate to be corrected by the CR measurements, and to be modified coherently with any systematic variations applied to the MC.

A likelihood is then constructed for the ensemble of measurements in the control regions as the product of Poisson distributions whose means are specified by the nominal MC estimate for that region, including the free normalisation factors μ_b [94]. For $\mu_{t\bar{t}}$ and μ_W , the corresponding leptonic control regions provide the constraints. The 6-jet ($j50$) or 5-jet ($j80$) template region is treated as another control region in the fit such that μ_{multijet} is coupled to any modifications of $\mu_{t\bar{t}}$ and μ_W . If $\mu_{t\bar{t}} = \mu_W = 1$, then $\mu_{\text{multijet}} = 1$ by construction, as the same region is used to derive the nominal multijet estimate. The systematic uncertainties (see Section 7.1) are implemented in the form of Gaussian-constrained nuisance parameters modifying the Poisson mean of each background component contributing to the estimate in a given signal or control region.

Minimisation of the likelihood (profiling) fixes the values of, and uncertainties on, μ_b , which can then be combined with the MC and template predictions to obtain the total background prediction in the signal region. The consistency between the background prediction and SR observation is computed in the form of a p -value CL_b which is the probability of an upwards fluctuation from the SR prediction no larger than that observed in data, given the background model.

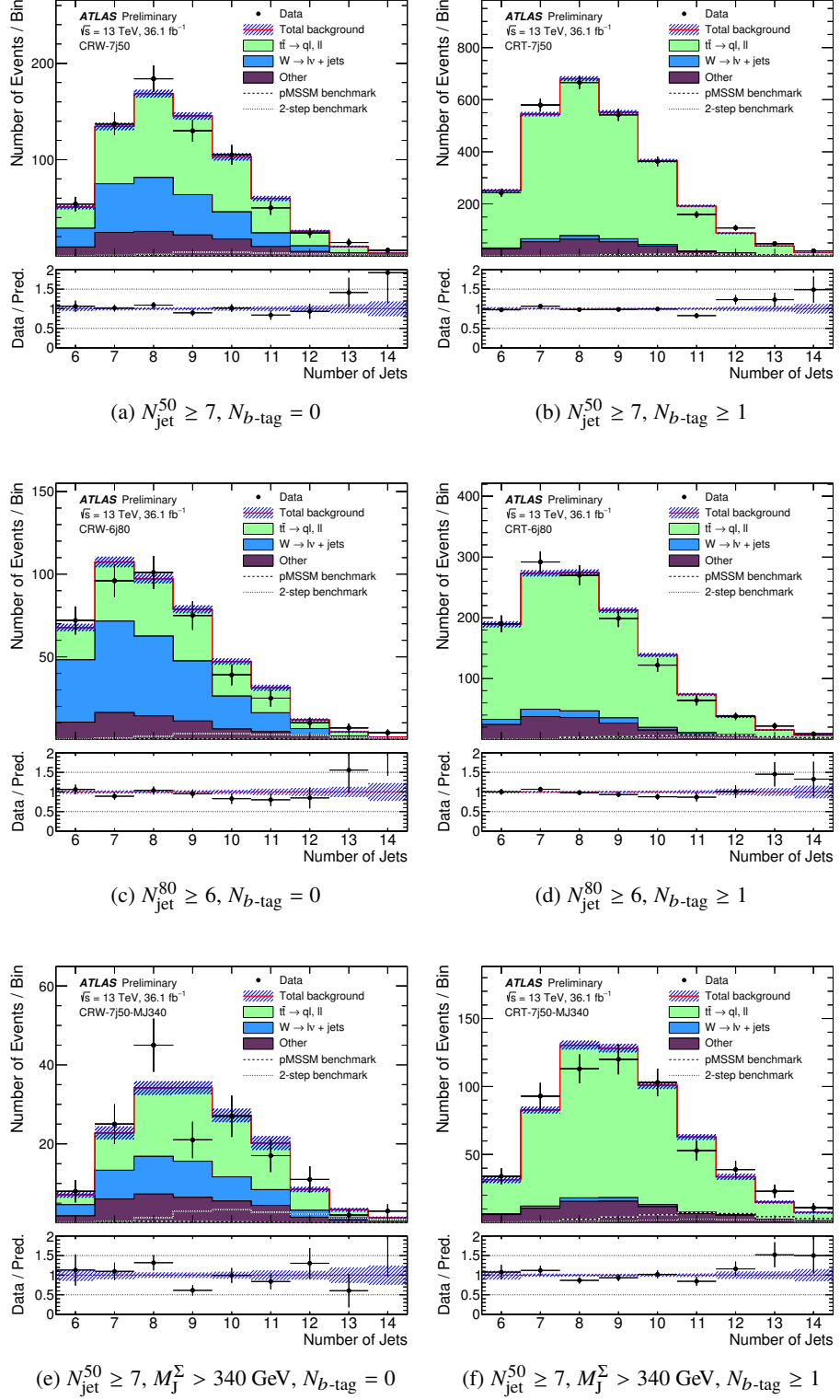


Figure 3: The distribution of the number of jets observed in the W +jets (left) and $t\bar{t}$ (right) control regions with the lowest jet multiplicities. The backgrounds have been scaled by the normalisation factors extracted from the fit, described in section 6.3. The blue hashed band indicates the statistical uncertainty from MC simulated samples. The dashed lines labelled ‘pMSSM’ and ‘2-step’ refer to benchmark signal points – a pMSSM slice model with $(m_{\tilde{g}}, m_{\tilde{\chi}_1^\pm}) = (1400, 200) \text{ GeV}$ and a cascade decay model with $(m_{\tilde{g}}, m_{\tilde{\chi}_1^0}) = (1400, 200) \text{ GeV}$. The lower panels show the ratio of the observed data to the total SM background.

7 Statistical procedures

7.1 Systematic uncertainties

Systematic uncertainties affecting this analysis are grouped into three sources:

Uncertainties from experimental sources include those on identification and reconstruction efficiencies, as well as energy and momentum scales and resolutions. They are assessed on all simulated event samples. Efficiency uncertainties are considered for hard-scatter jet selection, flavour tagging and selection of electrons and muons. Of these, only flavour-tagging systematics have a non-negligible effect on the total background expectation in the signal regions; at most 4% in the heavy-flavour-enriched SRs.

The energy/momentum uncertainties affect jets, electrons, muons and photons, and are furthermore propagated to the missing transverse momentum. Jet energy scale and resolution systematics contribute 6-12% to the total SR uncertainty. The soft term of the E_T^{miss} also has its own associated uncertainties, which in the jet mass channel may have up to an 8% effect. In this category also fall the uncertainty in the total integrated luminosity considered for analysis, as well as on the total inelastic pp cross-section, which affects the simulation of pileup (<1%).

Theoretical uncertainties on the event generation affect both background and signal MC samples. These are assessed by varying the matrix element and parton shower generators used, or by modifying scales (renormalisation, factorisation, resummation, matching) involved in the process calculations. Variation in the degree of additional radiation accompanying $t\bar{t}$ production is the single largest source of uncertainty in the SRs (10-25%); parton-shower uncertainties play a subdominant role, typically being half as large as but occasionally comparable to the radiation systematic. Due to their small overall effect on the analysis, constant uncertainties of 30% and 50% respectively are applied to the normalisation of diboson production and top-quark pair-production in association with vector bosons.

As described in Section 6.1, uncertainties are assessed on the multijet background estimates, where kinematic and flavour differences between the template and signal regions are considered. An additional overall systematic uncertainty is ascribed for general non-closure of the template prediction. Apart from in the jet-mass channel SRs, where the kinematic and flavour systematics are at most 3%, and in the most statistically-limited SRs, the three sources of uncertainty are similar in magnitude. Where the statistical precision is poorer, fluctuations can drive the non-closure uncertainty up to 18%.

7.2 Hypothesis testing

For interpretation of the signal region observations, the likelihood fits for background estimation (Section 6.3) are extended to perform two forms of hypothesis tests using a profile-likelihood-ratio test statistic [95], quantifying the significance of any observed excesses or the lack thereof. The discovery test discriminates between the null hypothesis stating that the SR measurement is consistent with only SM contributions and an alternative hypothesis postulating a positive signal. Conversely, any given signal model can be examined in an exclusion test of the signal-plus-background hypothesis, where an observation significantly smaller than the combination of SM and SUSY processes would lead to rejection of the signal model.

Taking into account all background predictions, normalisation factors and systematic uncertainties, the fit is implemented by including the SR in the ensemble of measurements and adding an additional signal

component solely in the SR. Using a profile likelihood test, the discovery p -value $p(s = 0)$ for a signal with strength 0 can be determined. This configuration also permits an upper limit on the visible signal cross-section to be set for an arbitrary signal, where no control region contamination is assumed.

Exclusion testing of a chosen signal model proceeds similarly, but a signal component is allowed in all control regions as well as the signal region, to correct for potential signal contamination (which has been verified to be small). Theoretical and experimental systematics on the signal MC are included in the fit. A profile-likelihood test is then made of the compatibility between the best-fit μ_{signal} from data and the nominal signal hypothesis, corresponding to a signal strength $\mu_{\text{signal}} = 1$. This provides the exclusion p -value $p(s = 1)$. Points in the SUSY parameter space are considered excluded if the CL_s parameter, computed as $p(s = 1)/(1 - CL_b)$, is smaller than 0.05 [96]. This protects against spurious exclusion of signals due to observing SR event counts significantly smaller than those predicted. While not strictly defining a frequentist confidence level, these are referred to as 95% CL limits.

8 Results and interpretation

The expected and observed event counts in the leptonic control regions are evaluated and normalisation factors derived. In general, the $t\bar{t}$ normalisation is close to 1 for lower jet multiplicities but may be as small as 0.71 for high jet multiplicities. For μ_W , the range is typically 0.3-0.6. Correspondingly, μ_{multijet} is corrected upwards by up to 24%.

Signal region yields as observed in data are summarised in Table 4. These are illustrated graphically in Figure 4. The largest discrepancy from the SM prediction is a deficit in the 9j MJ500 region with a statistical significance of 1.8 sigma and a corresponding p -value of 0.04. Similar deficits are observed in the other MJ SRs, but the large overlap between these SRs implies that the deficits are strongly correlated.

The full distributions of $E_T^{\text{miss}}/\sqrt{H_T}$ are shown for two indicative signal regions in Figure 5. For all signal regions, the data agree with the predicted $E_T^{\text{miss}}/\sqrt{H_T}$ distributions within the systematic uncertainties.

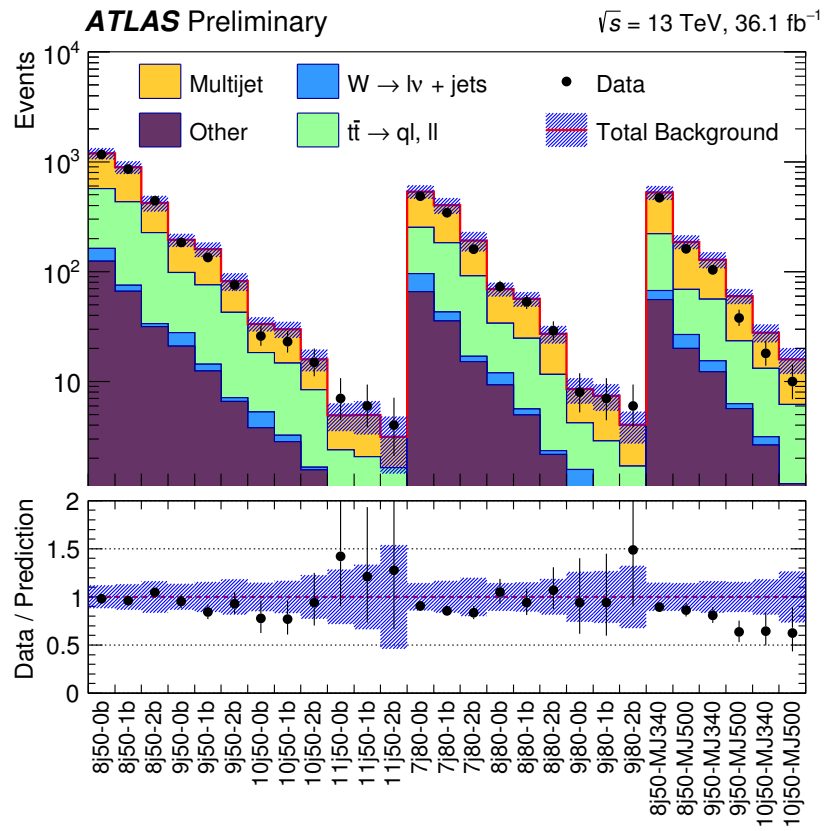


Figure 4: Summary plot showing the data and SM predictions constrained by the likelihood fit for all signal regions. Systematic and statistical uncertainties are shown in the blue hatched band, accounting for (anti-)correlations in their effects on different background components.

Signal region	Fitted background			Obs events	
	Multijet	Leptonic	Total		
$N_{\text{jet}}^{50} \geq 8$	$N_{\text{b-jet}} \geq 0$	622 ± 42	570 ± 140	1190 ± 140	1169
	$N_{\text{b-jet}} \geq 1$	460 ± 50	430 ± 110	890 ± 140	856
	$N_{\text{b-jet}} \geq 2$	196 ± 39	226 ± 57	422 ± 81	442
$N_{\text{jet}}^{50} \geq 9$	$N_{\text{b-jet}} \geq 0$	96 ± 11	98 ± 24	194 ± 28	185
	$N_{\text{b-jet}} \geq 1$	84 ± 15	76 ± 20	160 ± 31	135
	$N_{\text{b-jet}} \geq 2$	39 ± 12	42.5 ± 9.5	82 ± 19	76
$N_{\text{jet}}^{50} \geq 10$	$N_{\text{b-jet}} \geq 0$	15.1 ± 3.0	18.3 ± 3.9	33.5 ± 5.1	26
	$N_{\text{b-jet}} \geq 1$	15.3 ± 3.7	14.7 ± 3.3	30.0 ± 5.9	23
	$N_{\text{b-jet}} \geq 2$	7.6 ± 3.1	8.4 ± 1.8	16.0 ± 4.2	15
$N_{\text{jet}}^{50} \geq 11$	$N_{\text{b-jet}} \geq 0$	2.54 ± 0.76	2.4 ± 1.2	4.9 ± 1.2	7
	$N_{\text{b-jet}} \geq 1$	2.88 ± 0.84	2.1 ± 1.4	5.0 ± 1.3	6
	$N_{\text{b-jet}} \geq 2$	1.49 ± 0.72	1.6 ± 1.5	3.1 ± 1.5	4
$N_{\text{jet}}^{80} \geq 7$	$N_{\text{b-jet}} \geq 0$	282 ± 32	253 ± 69	535 ± 74	486
	$N_{\text{b-jet}} \geq 1$	219 ± 28	183 ± 60	402 ± 74	343
	$N_{\text{b-jet}} \geq 2$	100 ± 17	91 ± 34	191 ± 44	160
$N_{\text{jet}}^{80} \geq 8$	$N_{\text{b-jet}} \geq 0$	35.7 ± 5.6	33.8 ± 8.3	70 ± 10	73
	$N_{\text{b-jet}} \geq 1$	31.6 ± 5.7	24.8 ± 6.4	56 ± 10	53
	$N_{\text{b-jet}} \geq 2$	15.5 ± 3.8	11.6 ± 3.3	27.1 ± 6.0	29
$N_{\text{jet}}^{80} \geq 9$	$N_{\text{b-jet}} \geq 0$	4.3 ± 1.3	4.2 ± 1.8	8.5 ± 2.0	8
	$N_{\text{b-jet}} \geq 1$	4.5 ± 1.3	2.9 ± 1.5	7.4 ± 1.8	7
	$N_{\text{b-jet}} \geq 2$	2.34 ± 0.95	1.69 ± 0.89	4.0 ± 1.2	6
$N_{\text{jet}}^{50} \geq 8$	$M_J^\Sigma \geq 340 \text{ GeV}$	306 ± 54	220 ± 55	526 ± 72	471
	$M_J^\Sigma \geq 500 \text{ GeV}$	118 ± 18	69 ± 20	187 ± 24	161
$N_{\text{jet}}^{50} \geq 9$	$M_J^\Sigma \geq 340 \text{ GeV}$	73 ± 15	56 ± 15	129 ± 23	104
	$M_J^\Sigma \geq 500 \text{ GeV}$	36.5 ± 6.3	23.3 ± 7.0	60 ± 10	38
$N_{\text{jet}}^{50} \geq 10$	$M_J^\Sigma \geq 340 \text{ GeV}$	14.6 ± 3.8	13.2 ± 3.5	27.9 ± 5.7	18
	$M_J^\Sigma \geq 500 \text{ GeV}$	9.8 ± 2.6	6.2 ± 3.3	16.0 ± 4.7	10

Table 4: The expected SM background (and separately the multijet and leptonic contributions) and the observed number of data events. The SM background normalisations are obtained from fits to the data in control regions, as described in above.

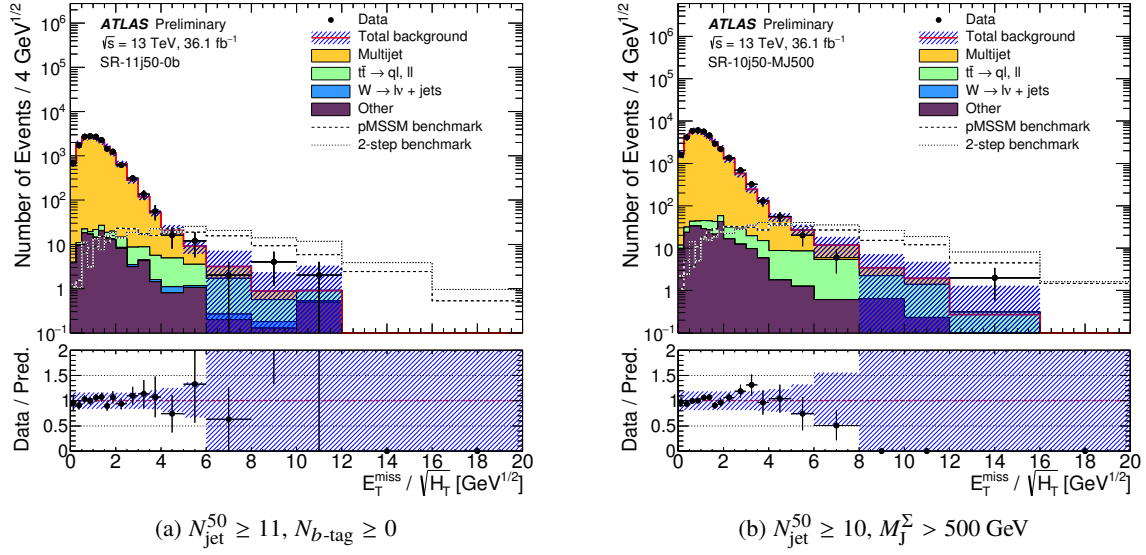


Figure 5: Distributions of the $E_T^{\text{miss}} / \sqrt{H_T}$ for events in the 11-jet SR for the 50 GeV flavour channel, inclusive in $N_{b\text{-tag}}$ (a) and the 10-jet SR for the jet mass channel (b), with $M_J^{\Sigma} > 500$ GeV. The backgrounds have been scaled by the normalisation factors extracted from the fit, described in section 6.3. The blue hashed band indicates the quadrature sum of the statistical uncertainty from MC simulated samples and the separate sources of systematic uncertainty on the background prediction. The dashed lines labelled ‘pMSSM’ and ‘2-step’ refer to benchmark signal points – a pMSSM slice model with $(m_{\tilde{g}}, m_{\tilde{\chi}^{\pm}}) = (1400, 200)$ GeV and a cascade decay model with $(m_{\tilde{g}}, m_{\tilde{\chi}_1^0}) = (1400, 200)$ GeV. The lower panels show the ratio of the observed data to the total SM background.

Table 5 quantifies the results of the fit to all signal regions. When testing for a positive signal, the smallest p_0 value observed is 0.2, for $N_{\text{jet}}^{80} \geq 9$ and $N_{b\text{-tag}} \geq 2$. The strongest limits set on the visible cross-section are of about 0.19 fb, for $N_{\text{jet}}^{50} \geq 11$ and $N_{b\text{-tag}} \geq 2$.

8.1 Exclusion limits

Using the exclusion configuration defined in Section 7.2, limits are set at the 95% CL in the signal scenarios described in Section 3.2.2. Constraints from all 27 SRs are combined by considering only the SR with the best expected exclusion sensitivity at every signal model point. These are illustrated in several parameter planes in Figures 6–7.

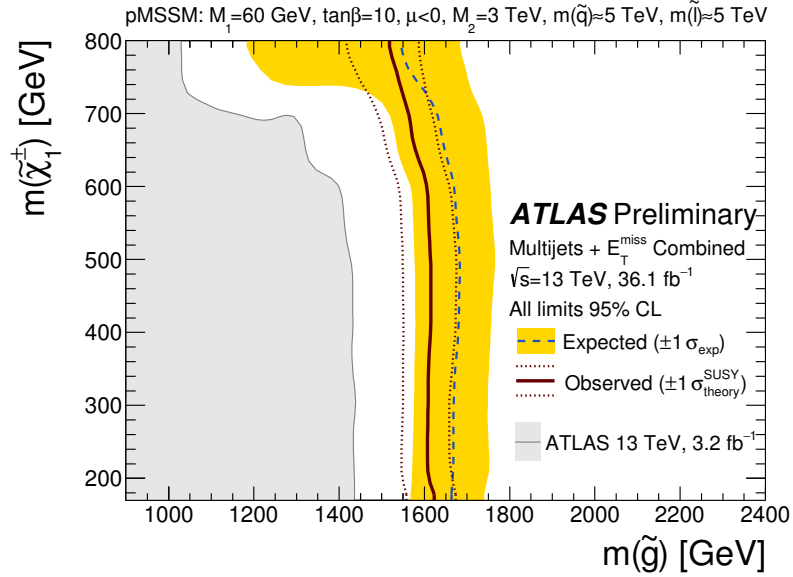
In the $m_{\tilde{g}}, m_{\tilde{\chi}_1^\pm}$ projection of the pMSSM, constraints are set such that $m_{\tilde{g}} \gtrsim 1600$ GeV, for $m_{\tilde{\chi}_1^\pm} < 600$ GeV is excluded. The limit falls to $m_{\tilde{g}} \gtrsim 1360$ GeV for $m_{\tilde{\chi}_1^\pm} \simeq 800$ GeV.

Limits are set up to $m_{\tilde{g}} \approx 1800$ GeV for small LSP masses when considering the simplified model assuming a two-step cascade decay of the gluino. For $m_{\tilde{g}} \simeq 800$ GeV, models are excluded provided that $m_{\tilde{\chi}_1^0} < 475$ GeV. The limits lie in the range $500 < m_{\tilde{\chi}_1^0} < 700$ GeV as the gluino mass increases to $m_{\tilde{g}} = 1600$ GeV.

Simplified models of gluino-mediated stop production are excluded for gluino masses up to 1500 GeV, as long as $m_{\tilde{\chi}_1^0} \lesssim 600$ GeV, when assuming that the stop is more massive than the gluino. When RPC restrictions are relaxed, gluino masses between 625 and 1400 GeV are excluded for $400 < m_{\tilde{\chi}_1^0} < 800$ GeV in a scenario where the stops decaying through an RPV coupling to $\bar{s}\bar{b}$.

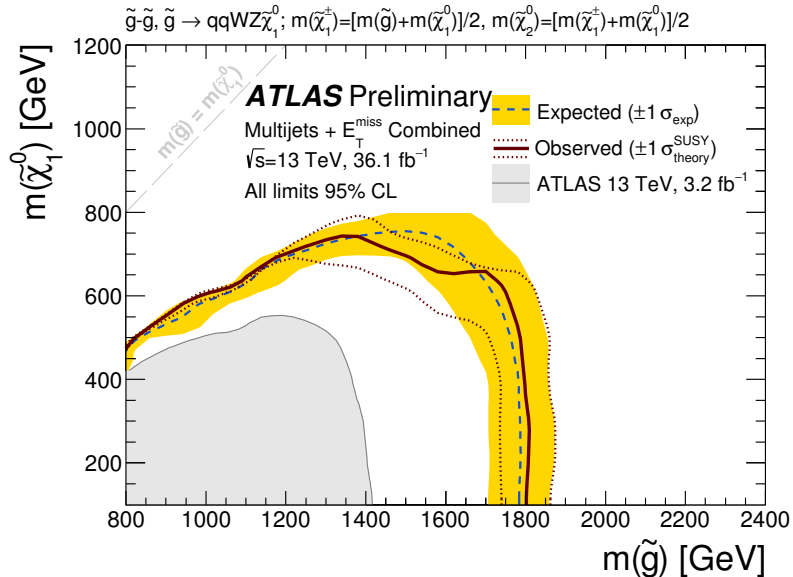
Signal Region		$\langle \epsilon \sigma \rangle_{\text{obs}}^{95}$ [fb]	S_{obs}^{95}	S_{exp}^{95}	$1 - CL_b$	$p(s = 0)$
$N_{\text{jet}}^{50} \geq 8$	$N_{\text{b-jet}} \geq 0$	7.2	260	270_{-70}^{+90}	0.44	0.50
	$N_{\text{b-jet}} \geq 1$	6.4	230	250_{-60}^{+80}	0.40	0.50
	$N_{\text{b-jet}} \geq 2$	4.6	170	160_{-40}^{+50}	0.59	0.40
$N_{\text{jet}}^{50} \geq 9$	$N_{\text{b-jet}} \geq 0$	1.5	53	58_{-15}^{+20}	0.38	0.50
	$N_{\text{b-jet}} \geq 1$	1.2	44	55_{-14}^{+18}	0.24	0.50
	$N_{\text{b-jet}} \geq 2$	1.0	35	38_{-9}^{+12}	0.40	0.50
$N_{\text{jet}}^{50} \geq 10$	$N_{\text{b-jet}} \geq 0$	0.30	11	15_{-4}^{+6}	0.17	0.50
	$N_{\text{b-jet}} \geq 1$	0.31	11	15_{-4}^{+6}	0.20	0.50
	$N_{\text{b-jet}} \geq 2$	0.31	11	12_{-3}^{+5}	0.44	0.50
$N_{\text{jet}}^{50} \geq 11$	$N_{\text{b-jet}} \geq 0$	0.23	8.5	$6.3_{-1.5}^{+3.0}$	0.80	0.21
	$N_{\text{b-jet}} \geq 1$	0.21	7.4	$6.5_{-1.7}^{+2.6}$	0.68	0.34
	$N_{\text{b-jet}} \geq 2$	0.19	6.9	$6.0_{-1.3}^{+2.2}$	0.69	0.35
$N_{\text{jet}}^{80} \geq 7$	$N_{\text{b-jet}} \geq 0$	3.1	110	130_{-30}^{+40}	0.27	0.50
	$N_{\text{b-jet}} \geq 1$	2.7	100	120_{-30}^{+40}	0.23	0.50
	$N_{\text{b-jet}} \geq 2$	1.7	60	72_{-17}^{+22}	0.26	0.50
$N_{\text{jet}}^{80} \geq 8$	$N_{\text{b-jet}} \geq 0$	0.80	29	27_{-7}^{+10}	0.60	0.40
	$N_{\text{b-jet}} \geq 1$	0.62	22	24_{-7}^{+9}	0.40	0.50
	$N_{\text{b-jet}} \geq 2$	0.49	18	16_{-5}^{+6}	0.59	0.41
$N_{\text{jet}}^{80} \geq 9$	$N_{\text{b-jet}} \geq 0$	0.22	7.8	$7.9_{-2.0}^{+3.4}$	0.47	0.50
	$N_{\text{b-jet}} \geq 1$	0.21	7.5	$7.5_{-2.1}^{+2.8}$	0.48	0.50
	$N_{\text{b-jet}} \geq 2$	0.22	8.0	$5.9_{-1.4}^{+2.6}$	0.81	0.20
$N_{\text{jet}}^{50} \geq 8$	$M_J^\Sigma \geq 340 \text{ GeV}$	2.9	100	130_{-30}^{+40}	0.24	0.50
	$M_J^\Sigma \geq 500 \text{ GeV}$	1.0	36	48_{-13}^{+17}	0.18	0.50
$N_{\text{jet}}^{50} \geq 9$	$M_J^\Sigma \geq 340 \text{ GeV}$	0.87	32	42_{-11}^{+14}	0.17	0.50
	$M_J^\Sigma \geq 500 \text{ GeV}$	0.32	12	20_{-6}^{+8}	0.04	0.50
$N_{\text{jet}}^{50} \geq 10$	$M_J^\Sigma \geq 340 \text{ GeV}$	0.25	9.1	14_{-4}^{+6}	0.10	0.50
	$M_J^\Sigma \geq 500 \text{ GeV}$	0.22	7.9	11_{-3}^{+4}	0.18	0.50

Table 5: Left to right: 95% CL upper limits on the visible cross section ($\langle \epsilon \sigma \rangle_{\text{obs}}^{95}$) and on the number of signal events (S_{obs}^{95}). The third column (S_{exp}^{95}) shows the 95% CL upper limit on the number of signal events, given the expected number (and $\pm 1\sigma$ excursions on the expectation) of background events. The last two columns indicate $1 - CL_b$, i.e. the complement of the p -value observed for the background-only hypothesis, and the discovery p -value ($p(s = 0)$).



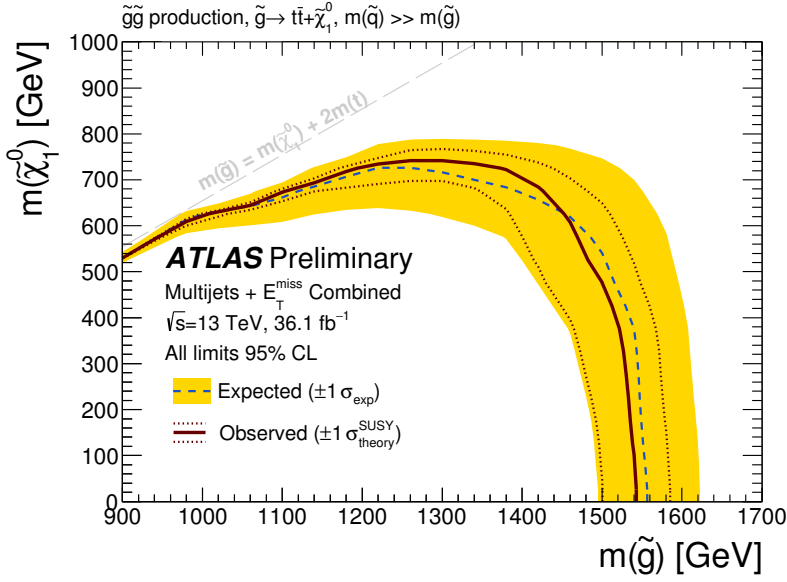
(a) pMSSM

c

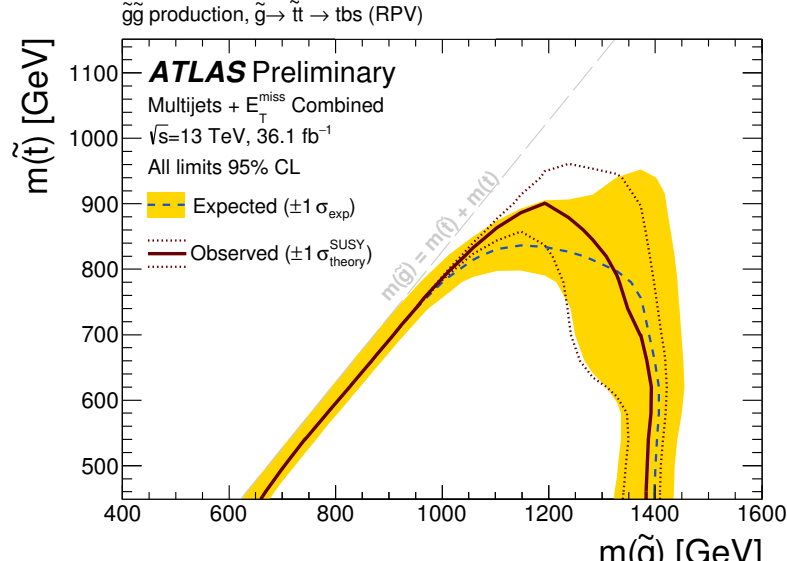


(b) Two-step decay

Figure 6: Exclusion contours in the $m_{\tilde{g}}, m_{\tilde{\chi}_1^\pm}$ plane for the pMSSM (a) and the $m_{\tilde{g}}, m_{\tilde{\chi}_1^0}$ plane in a simplified model with the gluino decaying via a two-step cascade (b). The solid maroon line indicates the observed limit, while the dashed blue line shows the expected limit. Experimental, MC theoretical and statistical uncertainties are shown in the yellow band. Dotted maroon lines delimit the variation of the observed limit within the $\pm 1\sigma$ uncertainties on the signal cross-section at NLO+NLL accuracy.



(a) Off-shell stops



(b) RPV

Figure 7: Exclusion contours in gluino-mediated stop production scenarios, illustrated in the $m_{\tilde{g}}$, $m_{\tilde{\chi}_1^0}$ plane with off-shell stops (a) and an R -parity-violating scenario plane in which the stop decays via $\tilde{t}_1 \rightarrow sb$ (b), shown in the $m_{\tilde{g}}$, $m_{\tilde{t}_1}$ plane. The solid maroon line indicates the observed limit, while the dashed blue line shows the expected limit. Experimental, MC theoretical and statistical uncertainties are shown in the yellow band. Dotted maroon lines delimit the variation of the observed limit within the $\pm 1\sigma$ uncertainties on the signal cross-section at NLO+NLL accuracy.

9 Conclusion

A search for heavy particles predicted by supersymmetric or other model beyond the SM decaying to produce large jet multiplicities in association with E_T^{miss} has been carried out using 36.1 fb^{-1} of $\sqrt{s} = 13 \text{ TeV}$ LHC pp collision data collected by ATLAS in 2015 and 2016. No significant excesses over the Standard Model background were observed in signal regions selecting up to 11 jets with $p_T > 50 \text{ GeV}$ or 9 jets with $p_T > 80 \text{ GeV}$. The largest jet multiplicity event observed in data had 13 jets with $p_T > 80 \text{ GeV}$, while the greatest observed jet mass sum was $M_J^{\Sigma} = 1.3 \text{ TeV}$.

Exclusion limits are placed on gluino production in supersymmetric signal scenarios with a range of model assumptions. The tightest limits are set at $m_{\tilde{g}} \approx 1800 \text{ GeV}$ in a simplified model assuming a two-step cascade decay via the $\tilde{\chi}_2^0$ and $\tilde{\chi}_1^{\pm}$. A slice of the phenomenological MSSM is excluded for $m_{\tilde{g}} < 1360 \text{ GeV}$, with tighter constraints at $m_{\tilde{g}} \approx 1600 \text{ GeV}$ for $m_{\tilde{\chi}_1^{\pm}} < 600 \text{ GeV}$. When assuming that the gluino decays through off-shell stops, masses of the gluino below 1500 GeV are excluded provided $m_{\tilde{\chi}_1^0} < 600 \text{ GeV}$. Limits are also set in an R-parity-violating model with baryon-number-violating couplings permitting $\tilde{t}_1 \rightarrow \bar{s}\bar{b}$, such that the gluino mass must be greater than 1250–1350 GeV when the stop mass is in the range $400 < m_{\tilde{t}_1} < 800 \text{ GeV}$.

References

- [1] L. Evans (ed.) and P. Bryant (ed.), *LHC Machine*, *JINST* **3** (2008) S08001.
- [2] G. R. Farrar and P. Fayet, *Phenomenology of the Production, Decay, and Detection of New Hadronic States Associated with Supersymmetry*, *Phys. Lett. B* **76** (1978) 575.
- [3] S. Wolfram, *Abundances of Stable Particles Produced in the Early Universe*, *Phys. Lett. B* **82** (1979) 65.
- [4] J. Rich, D. Lloyd Owen and M. Spiro, *EXPERIMENTAL PARTICLE PHYSICS WITHOUT ACCELERATORS*, *Phys. Rept.* **151** (1987) 239.
- [5] P. F. Smith, *Terrestrial Searches for New Stable Particles*, *Contemp. Phys.* **29** (1988) 159.
- [6] S. Abel and T. Falk, *Charge and color breaking in the constrained MSSM*, *Phys. Lett. B* **444** (1998) 427, arXiv: [hep-ph/9810297 \[hep-ph\]](#).
- [7] H. K. Dreiner, *An Introduction to explicit R-parity violation*, (1997), [Adv. Ser. Direct. High Energy Phys. 21, 565 (2010)], arXiv: [hep-ph/9707435 \[hep-ph\]](#).
- [8] ATLAS Collaboration, *The ATLAS Experiment at the CERN Large Hadron Collider*, *JINST* **3** (2008) S08003.
- [9] T. Cohen, E. Izaguirre, M. Lisanti and H. K. Lou, *Jet substructure by accident*, *JHEP* **03** (2013) 161, arXiv: [1212.1456 \[hep-ph\]](#).
- [10] ATLAS Collaboration, *Search for new phenomena in final states with large jet multiplicities and missing transverse momentum using $\sqrt{s} = 7 \text{ TeV}$ pp collisions with the ATLAS detector*, *JHEP* **11** (2011) 099, arXiv: [1110.2299 \[hep-ex\]](#).

- [11] ATLAS Collaboration, *Hunt for new phenomena using large jet multiplicities and missing transverse momentum with ATLAS in 4.7 fb^{-1} of $\sqrt{s} = 7 \text{ TeV}$ proton–proton collisions*, *JHEP* **07** (2012) 167, arXiv: [1206.1760 \[hep-ex\]](https://arxiv.org/abs/1206.1760).
- [12] ATLAS Collaboration, *Search for new phenomena in final states with large jet multiplicities and missing transverse momentum at $\sqrt{s} = 8 \text{ TeV}$ proton–proton collisions using the ATLAS experiment*, *JHEP* **10** (2013) 130, arXiv: [1308.1841 \[hep-ex\]](https://arxiv.org/abs/1308.1841).
- [13] ATLAS Collaboration, *Search for new phenomena in final states with large jet multiplicities and missing transverse momentum with ATLAS using $\sqrt{s} = 13 \text{ TeV}$ proton–proton collisions*, *Phys. Lett. B* **757** (2016) 334, arXiv: [1602.06194 \[hep-ex\]](https://arxiv.org/abs/1602.06194).
- [14] ATLAS Collaboration, *Summary of the searches for squarks and gluinos using $\sqrt{s} = 8 \text{ TeV}$ pp collisions with the ATLAS experiment at the LHC*, *JHEP* **10** (2015) 054, arXiv: [1507.05525 \[hep-ex\]](https://arxiv.org/abs/1507.05525).
- [15] ATLAS Collaboration, *Summary of the ATLAS experiment’s sensitivity to supersymmetry after LHC Run 1 — interpreted in the phenomenological MSSM*, *JHEP* **10** (2015) 134, arXiv: [1508.06608 \[hep-ex\]](https://arxiv.org/abs/1508.06608).
- [16] ATLAS Collaboration, *Search for squarks and gluinos in final states with jets and missing transverse momentum at $\sqrt{s} = 13 \text{ TeV}$ with the ATLAS detector*, *Eur. Phys. J. C* **76** (2016) 392, arXiv: [1605.03814 \[hep-ex\]](https://arxiv.org/abs/1605.03814).
- [17] ATLAS Collaboration, *Search for gluinos in events with an isolated lepton, jets and missing transverse momentum at $\sqrt{s} = 13 \text{ TeV}$ with the ATLAS detector*, *Eur. Phys. J. C* **76** (2016) 565, arXiv: [1605.04285 \[hep-ex\]](https://arxiv.org/abs/1605.04285).
- [18] ATLAS Collaboration, *Search for pair production of gluinos decaying via stop and sbottom in events with b-jets and large missing transverse momentum in pp collisions at $\sqrt{s} = 13 \text{ TeV}$ with the ATLAS detector*, *Phys. Rev. D* **94** (2016) 032003, arXiv: [1605.09318 \[hep-ex\]](https://arxiv.org/abs/1605.09318).
- [19] CMS Collaboration, *Search for supersymmetry in pp collisions at $\sqrt{s} = 8 \text{ TeV}$ in events with a single lepton, large jet multiplicity, and multiple b jets*, *Phys. Lett. B* **733** (2014) 328, arXiv: [1311.4937 \[hep-ex\]](https://arxiv.org/abs/1311.4937).
- [20] CMS Collaboration, *Searches for supersymmetry using the M_{T2} variable in hadronic events produced in pp collisions at 8 TeV*, *JHEP* **05** (2015) 078, arXiv: [1502.04358 \[hep-ex\]](https://arxiv.org/abs/1502.04358).
- [21] CMS Collaboration, *Search for stealth supersymmetry in events with jets, either photons or leptons, and low missing transverse momentum in pp collisions at 8 TeV*, *Phys. Lett. B* **743** (2015) 503, arXiv: [1411.7255 \[hep-ex\]](https://arxiv.org/abs/1411.7255).
- [22] CMS Collaboration, *Searches for supersymmetry based on events with b jets and four W bosons in pp collisions at 8 TeV*, *Phys. Lett. B* **745** (2015) 5, arXiv: [1412.4109 \[hep-ex\]](https://arxiv.org/abs/1412.4109).
- [23] CMS Collaboration, *Search for supersymmetry in the multijet and missing transverse momentum final state in pp collisions at 13 TeV*, *Phys. Lett. B* **758** (2016) 152, arXiv: [1602.06581 \[hep-ex\]](https://arxiv.org/abs/1602.06581).
- [24] CMS Collaboration, *Inclusive search for supersymmetry using razor variables in pp collisions at $\sqrt{s} = 13 \text{ TeV}$* , *Phys. Rev. D* **95** (2017) 012003, arXiv: [1609.07658 \[hep-ex\]](https://arxiv.org/abs/1609.07658).

[25] CMS Collaboration, *Search for supersymmetry in pp collisions at $\sqrt{s} = 13$ TeV in the single-lepton final state using the sum of masses of large-radius jets*, *JHEP* **08** (2016) 122, arXiv: [1605.04608 \[hep-ex\]](#).

[26] CMS Collaboration, *Phenomenological MSSM interpretation of CMS searches in pp collisions at $\sqrt{s} = 7$ and 8 TeV*, *JHEP* **10** (2016) 129, arXiv: [1606.03577 \[hep-ex\]](#).

[27] ATLAS Collaboration, *Performance of the ATLAS Trigger System in 2010*, *Eur. Phys. J. C* **72** (2012) 1849, arXiv: [1110.1530 \[hep-ex\]](#).

[28] ATLAS Collaboration, *Performance of the ATLAS Trigger System in 2015*, (2016), arXiv: [1611.09661 \[hep-ex\]](#).

[29] ATLAS Collaboration, *Luminosity determination in pp collisions at $\sqrt{s} = 8$ TeV using the ATLAS detector at the LHC*, *Eur. Phys. J. C* **76** (2016) 653, arXiv: [1608.03953 \[hep-ex\]](#).

[30] ATLAS Collaboration, *Characterisation and mitigation of beam-induced backgrounds observed in the ATLAS detector during the 2011 proton–proton run*, *JINST* **8** (2013) P07004, arXiv: [1303.0223 \[hep-ex\]](#).

[31] ATLAS Collaboration, *Selection of jets produced in 13 TeV proton–proton collisions with the ATLAS detector*, ATLAS-CONF-2015-029, 2015, URL: <https://cds.cern.ch/record/2037702>.

[32] T. Sjöstrand, S. Mrenna and P. Z. Skands, *A brief introduction to PYTHIA 8.1*, *Comput. Phys. Commun.* **178** (2008) 852, arXiv: [0710.3820 \[hep-ph\]](#).

[33] ATLAS Collaboration, *Summary of ATLAS Pythia 8 tunes*, ATL-PHYS-PUB-2012-003, 2012, URL: <https://cds.cern.ch/record/1474107>.

[34] A. D. Martin, W. J. Stirling, R. S. Thorne and G. Watt, *Parton distributions for the LHC*, *Eur. Phys. J. C* **63** (2009) 189, arXiv: [0901.0002 \[hep-ph\]](#).

[35] ATLAS Collaboration, *The ATLAS Simulation Infrastructure*, *Eur. Phys. J. C* **70** (2010) 823, arXiv: [1005.4568 \[hep-ex\]](#).

[36] GEANT4 Collaboration, S. Agostinelli et al., *GEANT4 – A simulation toolkit*, *Nucl. Instrum. Meth. A* **506** (2003) 250.

[37] ATLAS Collaboration, *Performance of the Fast ATLAS Tracking Simulation (FATRAS) and the ATLAS Fast Calorimeter Simulation (FastCaloSim) with single particles*, ATL-SOFT-PUB-2014-01, 2014, URL: <https://cds.cern.ch/record/1669341>.

[38] P. Nason, *A new method for combining NLO QCD with shower Monte Carlo algorithms*, *JHEP* **11** (2004) 040, arXiv: [hep-ph/0409146](#).

[39] S. Frixione, P. Nason and C. Oleari, *Matching NLO QCD computations with Parton Shower simulations: the POWHEG method*, *JHEP* **11** (2007) 070, arXiv: [0709.2092](#).

[40] S. Alioli, P. Nason, C. Oleari and E. Re, *A general framework for implementing NLO calculations in shower Monte Carlo programs: the POWHEG BOX*, *JHEP* **06** (2010) 043, arXiv: [1002.2581 \[hep-ph\]](#).

- [41] S. Alioli, P. Nason, C. Oleari and E. Re,
NLO single-top production matched with shower in POWHEG: s- and t-channel contributions, **JHEP** **09** (2009) 111, [Erratum: JHEP02,011(2010)], arXiv: [0907.4076 \[hep-ph\]](#).
- [42] E. Re,
Single-top Wt-channel production matched with parton showers using the POWHEG method, **Eur. Phys. J.** **C71** (2011) 1547, arXiv: [1009.2450 \[hep-ph\]](#).
- [43] S. Alioli, S.-O. Moch and P. Uwer,
Hadronic top-quark pair-production with one jet and parton showering, **JHEP** **01** (2012) 137, arXiv: [1110.5251 \[hep-ph\]](#).
- [44] H.-L. Lai et al., *New parton distributions for collider physics*, **Phys. Rev. D** **82** (2010) 074024, arXiv: [1007.2241 \[hep-ph\]](#).
- [45] P. Artoisenet, R. Frederix, O. Mattelaer and R. Rietkerk,
Automatic spin-entangled decays of heavy resonances in Monte Carlo simulations, **JHEP** **03** (2013) 015, arXiv: [1212.3460 \[hep-ph\]](#).
- [46] T. Sjöstrand, S. Mrenna and P. Z. Skands, *PYTHIA 6.4 physics and manual*, **JHEP** **05** (2006) 026, arXiv: [hep-ph/0603175](#).
- [47] J. Pumplin et al.,
New generation of parton distributions with uncertainties from global QCD analysis, **JHEP** **07** (2002) 012, arXiv: [hep-ph/0201195 \[hep-ph\]](#).
- [48] P. Z. Skands, *Tuning Monte Carlo generators: The Perugia tunes*, **Phys. Rev. D** **82** (2010) 074018, arXiv: [1005.3457 \[hep-ph\]](#).
- [49] D. J. Lange, *The EvtGen particle decay simulation package*, **Nucl. Instrum. Meth. A** **462** (2001) 152.
- [50] M. Czakon and A. Mitov,
Top++: a program for the calculation of the top-pair cross-section at hadron colliders, **Comput. Phys. Commun.** **185** (2014) 2930, arXiv: [1112.5675 \[hep-ph\]](#).
- [51] J. Alwall et al., *The automated computation of tree-level and next-to-leading order differential cross sections, and their matching to parton shower simulations*, **JHEP** **07** (2014) 079, arXiv: [1405.0301 \[hep-ph\]](#).
- [52] ATLAS Collaboration, *ATLAS Pythia 8 tunes to 7 TeV data*, ATL-PHYS-PUB-2014-021, 2014, URL: <https://cds.cern.ch/record/1966419>.
- [53] NNPDF Collaboration, R. D. Ball et al., *Parton distributions with LHC data*, **Nucl. Phys. B** **867** (2013) 244, arXiv: [1207.1303 \[hep-ph\]](#).
- [54] NNPDF Collaboration, R. D. Ball et al., *Parton distributions for the LHC run II*, **Journal of High Energy Physics** **2015** (2015) 1, ISSN: 1029-8479, arXiv: [1410.8849 \[hep-ph\]](#), URL: [http://dx.doi.org/10.1007/JHEP04\(2015\)040](http://dx.doi.org/10.1007/JHEP04(2015)040).
- [55] T. Gleisberg and S. Hoeche, *Comix, a new matrix element generator*, **JHEP** **12** (2008) 039, arXiv: [0808.3674 \[hep-ph\]](#).
- [56] F. Caccioli, P. Maierhöfer and S. Pozzorini, *Scattering Amplitudes with Open Loops*, **Phys. Rev. Lett.** **108** (2012) 111601, arXiv: [1111.5206 \[hep-ph\]](#).

- [57] S. Schumann and F. Krauss,
A Parton shower algorithm based on Catani-Seymour dipole factorisation, **JHEP** **03** (2008) 038, arXiv: [0709.1027 \[hep-ph\]](#).
- [58] S. Hoeche, F. Krauss, M. Schonherr and F. Siegert,
QCD matrix elements + parton showers: The NLO case, **JHEP** **04** (2013) 027, arXiv: [1207.5030 \[hep-ph\]](#).
- [59] T. Gleisberg et al., *Event generation with SHERPA 1.1*, **JHEP** **02** (2009) 007, arXiv: [0811.4622 \[hep-ph\]](#).
- [60] ATLAS Collaboration, *Comparison of Monte Carlo generator predictions from Powheg and Sherpa to ATLAS measurements of top pair production at 7 TeV*, ATL-PHYS-PUB-2015-011, 2015, URL: <https://cds.cern.ch/record/2020602>.
- [61] M. Bähr et al., *Herwig++ physics and manual*, **Eur. Phys. J. C** **58** (2008) 639, arXiv: [0803.0883 \[hep-ph\]](#).
- [62] ATLAS Collaboration, *Multi-boson simulation for 13 TeV ATLAS analyses*, ATL-PHYS-PUB-2016-002, 2016, URL: <https://cds.cern.ch/record/2119986>.
- [63] ATLAS Collaboration, *Monte Carlo Generators for the Production of a W or Z/ γ^* Boson in Association with Jets at ATLAS in Run 2*, ATL-PHYS-PUB-2016-003, 2016, URL: <https://cds.cern.ch/record/2120133>.
- [64] ATLAS Collaboration,
Simulation of top-quark production for the ATLAS experiment at $\sqrt{s} = 13$ TeV, ATL-PHYS-PUB-2016-004, 2016, URL: <https://cds.cern.ch/record/2120417>.
- [65] ATLAS Collaboration,
Modelling of the $t\bar{t}H$ and $t\bar{t}V$ ($V = W, Z$) processes for $\sqrt{s} = 13$ TeV ATLAS analyses, ATL-PHYS-PUB-2016-005, 2016, URL: <https://cds.cern.ch/record/2120826>.
- [66] A. Djouadi et al., *The Minimal supersymmetric standard model: Group summary report*, (1998), arXiv: [hep-ph/9901246](#).
- [67] C. F. Berger, J. S. Gainer, J. L. Hewett and T. G. Rizzo, *Supersymmetry without prejudice*, **JHEP** **02** (2009) 023, arXiv: [0812.0980 \[hep-ph\]](#).
- [68] B. C. Allanach, *SOFTSUSY: a program for calculating supersymmetric spectra*, **Comput. Phys. Commun.** **143** (2002) 305, arXiv: [hep-ph/0104145](#).
- [69] A. Djouadi, M. Mühlleitner and M. Spira, *Decays of supersymmetric particles: The Program SUSY-HIT (SUspect-SdecaY-Hdecay-Interface)*, **Acta Phys. Polon. B** **38** (2007) 635, arXiv: [hep-ph/0609292](#).
- [70] L. Lonnblad, *Correcting the color dipole cascade model with fixed order matrix elements*, **JHEP** **05** (2002) 046, arXiv: [hep-ph/0112284 \[hep-ph\]](#).
- [71] W. Beenakker, R. Höpkerb, M. Spirac and P. M. Zerwas,
Squark and gluino production at hadron colliders, **Nucl.Phys. B** **492** (1997) 51, arXiv: [hep-ph/9610490 \[hep-ph\]](#).
- [72] A. Kulesza and L. Motyka,
Threshold resummation for squark-antisquark and gluino-pair production at the LHC, **Phys. Rev. Lett.** **102** (2009) 111802, arXiv: [0807.2405 \[hep-ph\]](#).

[73] A. Kulesza and L. Motyka, *Soft gluon resummation for the production of gluino-gluino and squark-antisquark pairs at the LHC*, *Phys. Rev. D* **80** (2009) 095004, arXiv: [0905.4749 \[hep-ph\]](#).

[74] W. Beenakker, S. Brensing, M. Kramer, A. Kulesza, E. Laenen et al., *Soft-gluon resummation for squark and gluino hadroproduction*, *JHEP* **12** (2009) 041, arXiv: [0909.4418 \[hep-ph\]](#).

[75] W. Beenakker, S. Brensing, M. Kramer, A. Kulesza, E. Laenen et al., *Squark and gluino hadroproduction*, *Int. J. Mod. Phys. A* **26** (2011) 2637, arXiv: [1105.1110 \[hep-ph\]](#).

[76] C. Borschensky et al., *Squark and gluino production cross sections in pp collisions at $\sqrt{s} = 13, 14, 33$ and 100 TeV*, *Eur. Phys. J. C* **74** (2014) 3174, arXiv: [1407.5066 \[hep-ph\]](#).

[77] ATLAS Collaboration, *Vertex Reconstruction Performance of the ATLAS Detector at $\sqrt{s} = 13$ TeV*, ATL-PHYS-PUB-2015-026, 2015, URL: <https://cds.cern.ch/record/2037717>.

[78] ATLAS Collaboration, *Topological cell clustering in the ATLAS calorimeters and its performance in LHC Run 1*, (2016), arXiv: [1603.02934 \[hep-ex\]](#).

[79] M. Cacciari, G. P. Salam and G. Soyez, *The anti- k_t jet clustering algorithm*, *JHEP* **04** (2008) 063, arXiv: [0802.1189 \[hep-ph\]](#).

[80] M. Cacciari, G. P. Salam and G. Soyez, *FastJet user manual*, *Eur. Phys. J. C* **72** (2012) 1896, arXiv: [1111.6097 \[hep-ph\]](#).

[81] M. Cacciari and G. P. Salam, *Pileup subtraction using jet areas*, *Phys. Lett. B* **659** (2008) 119, arXiv: [0707.1378 \[hep-ph\]](#).

[82] M. Aaboud et al., *Jet energy scale measurements and their systematic uncertainties in proton-proton collisions at $\sqrt{s} = 13$ TeV with the ATLAS detector*, (2017), arXiv: [1703.09665 \[hep-ex\]](#).

[83] ATLAS Collaboration, *Performance of pile-up mitigation techniques for jets in pp collisions at $\sqrt{s} = 8$ TeV using the ATLAS detector*, *Eur. Phys. J. C* **76** (2016) 581, arXiv: [1510.03823 \[hep-ex\]](#).

[84] ATLAS Collaboration, *Optimisation of the ATLAS b-tagging performance for the 2016 LHC Run*, ATL-PHYS-PUB-2016-012, 2016, URL: <https://cds.cern.ch/record/2160731>.

[85] ATLAS Collaboration, *Performance of b-jet identification in the ATLAS experiment*, *JINST* **11** (2016) P04008, arXiv: [1512.01094 \[hep-ex\]](#).

[86] B. Nachman, P. Nef, A. Schwartzman, M. Swiatlowski and C. Wanotayaroj, *Jets from Jets: Re-clustering as a tool for large radius jet reconstruction and grooming at the LHC*, *JHEP* **02** (2015) 075, arXiv: [1407.2922 \[hep-ph\]](#).

[87] ATLAS Collaboration, *Electron reconstruction and identification efficiency measurements with the ATLAS detector using the 2011 LHC proton–proton collision data*, *Eur. Phys. J. C* **74** (2014) 2941, arXiv: [1404.2240 \[hep-ex\]](#).

[88] ATLAS Collaboration, *Measurement of the photon identification efficiencies with the ATLAS detector using LHC Run-1 data*, *Eur. Phys. J. C* **76** (2016) 666, arXiv: [1606.01813 \[hep-ex\]](#).

- [89] ATLAS Collaboration, *Electron and photon energy calibration with the ATLAS detector using LHC Run 1 data*, *Eur. Phys. J. C* **74** (2014) 3071, arXiv: [1407.5063 \[hep-ex\]](https://arxiv.org/abs/1407.5063).
- [90] ATLAS Collaboration, *Electron efficiency measurements with the ATLAS detector using 2012 LHC proton–proton collision data*, *Eur. Phys. J. C* **77** (2017) 195, arXiv: [1612.01456 \[hep-ex\]](https://arxiv.org/abs/1612.01456).
- [91] ATLAS Collaboration, *Muon reconstruction performance of the ATLAS detector in proton–proton collision data at $\sqrt{s} = 13$ TeV*, *Eur. Phys. J. C* **76** (2016) 292, arXiv: [1603.05598 \[hep-ex\]](https://arxiv.org/abs/1603.05598).
- [92] ATLAS Collaboration, *Muon reconstruction performance in early $\sqrt{s} = 13$ TeV data*, ATL-PHYS-PUB-2015-037, 2015, URL: <https://cds.cern.ch/record/2047831>.
- [93] ATLAS Collaboration, *Performance of algorithms that reconstruct missing transverse momentum in $\sqrt{s} = 8$ TeV proton–proton collisions in the ATLAS detector*, *Eur. Phys. J. C* **77** (2017) 241, arXiv: [1609.09324 \[hep-ex\]](https://arxiv.org/abs/1609.09324).
- [94] Baak, M. and Besjes, G. J. and Côte, D. and Koutsman, A. and Lorenz, J. and Short, D., *HistFitter software framework for statistical data analysis*, *Eur. Phys. J. C* **75** (2015) 153, arXiv: [1410.1280 \[hep-ex\]](https://arxiv.org/abs/1410.1280).
- [95] G. Cowan, K. Cranmer, E. Gross and O. Vitells, *Asymptotic formulae for likelihood-based tests of new physics*, *Eur. Phys. J. C* **71** (2011) 1554, arXiv: [1007.1727 \[physics.data-an\]](https://arxiv.org/abs/1007.1727).
- [96] A. Read, *Presentation of search results: the CL_s technique*, *J. Phys. G* **28** (2002) 2693.